THE UNIVERSITY of EDINBURGH

Edinburgh Research Explorer

A cell/cilia cycle biosensor for single cell kinetics reveals persistence of cilia after the G1/ S transition is a general property in cells and mice

Citation for published version:
Ford, MJ, Yeyati, P, Mali, G, Keighren, M, Waddell, S, Mjoseng, HK, Douglas, AT, Hall, E, Sakaue-Sawano, A, Miyawaki, A, Meehan, R, Boulter, L, Jackson, I, Mill, P & Mort, R 2018, 'A cell/cilia cycle biosensor for single cell kinetics reveals persistence of cilia after the G1/ S transition is a general property in cells and mice' Developmental Cell. DOI: 10.1016/j.devcel.2018.10.027

Digital Object Identifier (DOI):
10.1016/j.devcel.2018.10.027

Link:
Link to publication record in Edinburgh Research Explorer

Document Version:
Peer reviewed version

Published In:
Developmental Cell

General rights
Copyright for the publications made accessible via the Edinburgh Research Explorer is retained by the author(s) and / or other copyright owners and it is a condition of accessing these publications that users recognise and abide by the legal requirements associated with these rights.

Take down policy
The University of Edinburgh has made every reasonable effort to ensure that Edinburgh Research Explorer content complies with UK legislation. If you believe that the public display of this file breaches copyright please contact openaccess@ed.ac.uk providing details, and we will remove access to the work immediately and investigate your claim.

OPEN ACCESS

Download date: 05. Apr. 2019

A cell/cilia cycle biosensor for single cell kinetics reveals persistence of cilia after the G1/S transition is a general property in cells and mice

Matthew J. Ford [1*, †], Patricia L. Yeyati [1, †], Girish R. Mali [1], Margaret A. Keighren [1], Scott H. Waddell [1], Heidi K. Mjoseng [1], Adam T. Douglas [1], Emma A. Hall [1], Asako Sakaue-Sawano [2], Atsushi Miyawaki [2], Richard R. Meehan [1], Luke Boulter [1], Ian J. Jackson [1, 3], Pleasantine Mill [1, ‡] and Richard L. Mort.[4, 5, ‡]

1. MRC Human Genetics Unit, MRC Institute of Genetics & Molecular Medicine, University of Edinburgh, Western General Hospital, Edinburgh, EH4 2XU, UK

2. Laboratory for Cell Function and Dynamics, Centre of Brain Science, RIKEN, 2-1 Hirosawa, Wako-city, Saitama, 351-0198, Japan

3. Roslin Institute, University of Edinburgh, Roslin, EH25 9RG, UK

4. Division of Biomedical and Life Sciences, Faculty of Health and Medicine, Furness Building, Lancaster University, Bailrigg, Lancaster, LA1 4YG, UK

5. Lead contact: r.mort@lancaster.ac.uk

* Currently affiliated with the Goodman Cancer Research Centre, McGill University, Montreal, Quebec, H3A 1A3, Canada

† These authors contributed equally

‡ Correspondence: r.mort@lancaster.ac.uk, pleasantine.mill@igmm.ed.ac.uk

Summary

The cilia and cell cycles are inextricably linked. Centrioles in the basal body of cilia nucleate the ciliary axoneme and sequester pericentriolar matrix (PCM) at the centrosome to organise the mitotic spindle. Cilia themselves respond to growth signals, prompting cilia resorption and cell cycle re-entry. We describe a fluorescent cilia and cell cycle biosensor allowing live imaging of cell cycle progression and cilia assembly/disassembly kinetics in cells and inducible mice. We define assembly and disassembly in relation to cell cycle stage with single cell resolution and explore the intercellular heterogeneity in cilia kinetics. In all cells and tissues analysed we observed cilia that persist through the G1/S transition and into S/G2/M-phase. We conclude that persistence of cilia after the G1/S transition is a general property. This new resource will shed light at an individual cell level on the interplay between the cilia and cell cycles in development, regeneration and disease.

Keywords

Cilia, cell cycle, reporter mouse, *Rosa26*, live imaging, biosensor

Introduction

Cilia are microtubule-based cellular projections that come in motile and non-motile forms. They sense key mechanical and environmental cues including the transduction of mitogenic signals that include Hedgehog (HH), insulin-like growth factor 1 (IGF-1) and platelet-derived growth factor (PDGF) (Goetz and Anderson, 2010). Defects in cilia result in a broad group of disorders termed ciliopathies. The structural and functional diversity of mammalian cilia likely underlies the huge spectrum of phenotypes observed in ciliopathy patients (Reiter and Leroux, 2017). We currently know very little about cell type-specific and developmental stage-specific differences in cilia dynamics and their interplay with the cell cycle during tissue morphogenesis and disease.

Primary cilia are dynamic organelles whose assembly and resorption are inextricably coupled with cell cycle progression. Evidence connecting primary cilia and the cell cycle, from mostly cell culture studies, suggests that primary cilia may function as a structural checkpoint guarding against cell cycle re-entry (Izawa *et al.*, 2015). The spatially distinct dual functions of the centrioles as structural components of both the basal body of the cilium and centrosomes at the poles of the mitotic spindle likely contributes to this coordination. The basal body must be disassembled prior to mitosis in order for the spindle to form and then differentiates in the subsequent cell cycle, enabling it to dock to the plasma membrane and form the ciliary axoneme (reviewed in Seeley & Nachury, 2010). Evidence also exists for extensive molecular crosstalk between ciliary factors and key cell cycle regulators; for example APC (Anaphase Promoting Complex), may be sequestered at the cilium and localised cell-cycle dependent proteolysis of the CDK5-SCF-Nde1 axis may trigger cell cycle progression (Maskey et al., 2015; Pugacheva et al., 2007; Wang et al., 2014).

In disease, the interplay between the cilia and cell cycles is complex. The presence of cilia is antiproliferative in some cases of cancer and polycystic kidney disease (Lin *et al.*, 2003; Jonassen *et al.*, 2008; Hassounah *et al.*, 2013; Menzl *et al.*, 2014; Phua *et al.*, 2017).

Conversely, proproliferative ciliary dependent signalling through the HH and Wnt pathways can drive the development of cancer (Han et al., 2009; Ma et al., 2013; Wong et al., 2009). Furthermore, there are causative links between the mis-regulation of cilia length and stability and kinase inhibitor resistance in cancer (Jenks et al., 2018). These examples highlight the translational importance of better understanding cilia dynamics and signalling in cell type and disease specific contexts.

Clearly strategies for parallel analysis of cell cycle progression and ciliary parameters *in vivo* are required to advance many fields. The Fucci2 (Fluorescent Ubiquitination-based Cell Cycle Indicator) system consists of cell cycle biosensors incorporating truncated forms of the human cell cycle phase specific proteins CDT1 (amino acids 30-120) and Geminin (amino acids 1-110) and the fluorescent proteins mCherry and mVenus respectively (Sakaue-Sawano *et al.*, 2008; Abe *et al.*, 2013). *R26Fucci2aR* is a Cre-inducible cell cycle reporter mouse that incorporates the Fucci2 probes fused with the *Thosea asigna* virus 2A self-cleaving peptide sequence in a single bicistronic construct (Mort *et al.*, 2014).

The ciliary protein ARL13B is a small GTPase enriched in cilia and is required for cilium assembly and HH signalling (Caspary, Larkins and Anderson, 2007). *ARL13B* mutations are causal in a subset of patients with classical Joubert syndrome (JS, MIM:608922); characterised by abnormal MRI, ataxia, psychomotor delay and cerebellar vermis hypoplasia. Overexpression of wild-type human ARL13B is tolerated in zebrafish and can rescue the JS-like phenotype in *arl13b*^{sco} mutants (Cantagrel *et al.*, 2008). Several transgenic models exist that label primary and motile cilia by fusion of wild-type ARL13B to fluorescent proteins (Borovina *et al.*, 2010; Delling *et al.*, 2013; Bangs *et al.*, 2015; Schmitz *et al.*, 2017). These models exhibit no adverse gross phenotypes; Shh signalling is not affected, embryos and tissues develop normally and animals are healthy. However, consistent with ARL13B's function in extending the ciliary axoneme and membrane, increased ciliary length has been reported upon ARL13B overexpression (Larkins *et*

al., 2011; Lu *et al.*, 2015; Pintado *et al.*, 2015). Furthermore abnormal periciliary mislocalisation has been observed on ARL-13::GFP overexpression in *C. elegans* (Warburton-Pitt *et al.*, 2014).

Here we report the design, construction and validation of a tricistronic cilia and cell cycle biosensor incorporating ARL13B-Cerulean and Fucci2a and the development of a Cre-inducible *R26Arl13b-Fucci2aR* reporter mouse. The model we have generated allows capture of high-resolution images enabling identification of the cell cycle stage and ciliation state of individual cells in culture and in all tissues examined, both embryonic and adult. The *R26Arl13b-Fucci2aR* mouse is a powerful new tool for the understanding of cilia and cell cycle kinetics during mouse development and disease progression.

Design:

An Arl13bCerulean-Fucci2a tricistronic biosensor designed to label the cilia and cell cycles

In order to design a multicistronic construct to visualise cilia and cell cycle kinetics that could be expressed from a single locus in mice, we took advantage of the optimal spectral separation of mCerulean from the fluorescent components of the Fucci2a system; mCherry and mVenus (Rizzo et al., 2004; Shaner et al., 2005). We fused the full mouse *Arl13b* cDNA (OTTMUST00000058920.GRCm38) to mCerulean and coupled this construct to Fucci2a (Figure 1A), with expression driven by the CAG synthetic promoter (Miyazaki et al., 1989). To confirm that the construct was bright enough in single copy number we tested it in NIH 3T3 cells by incorporating a single copy of CAG-Arl13bCerulean-Fucci2a using the Flp/In system (Thermofisher, Massachusetts, USA) to generate a stable isogenic cell line (Figure 1A). We observed normal cell-cycle progression and the correct localisation of the Fucci2a probes to the nucleus (Figure 1B). mCherry-hCdt1(30/120) and mVenus-hGem(1/110) fluorescence correlated with the G1 and S/G2/M cell cycle phases respectively in our time-lapse sequences (Movie S1 left panel). Cell cycle phase specificity of the Fucci2a probes was further confirmed by DNA content quantification using FACS (Figure 1C-E). In parallel we observed primary cilia clearly

labelled by ARL13B-Cerulean during cell cycle progression and as cells became confluent (Figure 1B and Movie S1). The proportion of ciliated cells varied with the proportion of cells in the Fucci2a labelled cell cycle phases. Typically, in subconfluent cultures 8.8 ± 2.87% of cells in G1 (n = 165 cells) were ciliated whilst in S/G2/M 11.0 ± 3.82% of cells (n = 119 cells) where ciliated. In confluent cultures 66.1 ± 4.47% (n = 256 cells) and 73.0 ± 15.58% of cells (n = 23 cells) were ciliated in G1 and S/G2/M phases respectively. We could resolve cilia at all stages of the cell cycle. In confluent cultures cilia ranged in length from 2.52 µm to 21.38 µm; the mean (± 95% CI) length was 7.07 ± 0.33 µm (n = 221 cells). These data show that Arl13bCerulean-Fucci2a is bright enough as a single copy number insertion for us to resolve both the cell cycle stage specific abundance of the Fucci2a probes and the localisation of ARL13B-Cerulean to the primary cilia using live confocal microscopy.

Generation of *R26Ar13b-Fucci2aR* inducible cell and cilia cycle reporter mice

R26Arl13b-Fucci2aR mice were generated by targeting a Cre-recombinase inducible version of Arl13bCerulean-Fucci2a to the *Rosa26* locus via homologous recombination in mESCs (Soriano, 1999) (Figure S1A-D and Methods). Upon Cre-activation (see Methods) we were able to identify cell cycle phase by differential abundance of the Fucci2a probes and primary cilia labelled with ARL13B-Cerulean under 2i culture conditions (Figure S1D) in agreement with previous reports (Bangs et al., 2015). *R26Arl13b-Fucci2aR* mice were generated by blastocyst injection of correctly targeted *R26Arl13b-Fucci2aR* ES cells (MGI: 6193732). No expression of the transgene was detected by fluorescent imaging confirming the functionality of the neomycin stop cassette (data not shown). To screen for abnormal phenotypes a constitutive mouse line (*R26Arl13b-Fucci2a,* MGI: 6193734,) was generated by crossing with ubiquitous *CAG-Cre* animals (unpublished – provided by Dr D. A. Kleinjan, University of Edinburgh) to delete the floxed neomycin stop cassette. In a cross to breed away the Cre-transgene *R26Arl13b-Fucci2a* mice were born at Mendelian ratios (n = 15, 26 and 10 wild type, *R26Arl13b-Fucci2a*$^{+/Tg}$ *and R26Arl13b-Fucci2a*$^{Tg/Tg}$ animals respectively, 2 tailed Chi-squared *P* = 0.6065). *R26Arl13b-Fucci2a*$^{Tg/Tg}$ animals were fertile and grossly phenotypically indistinguishable from wild type

littermates (Figure S1E,F). Bangs et al (2015) reported an increase in ciliary length of 37% in mCherry-ARL13B mice without any observed phenotypic consequences. Here we observed a similar, significant 1.48x increase in ciliary length in *R26Arl13b-Fucci2a*$^{Tg/Tg}$ MEFs compared to wild type MEFs (Figure S2A-B) but not in motile multiciliated nasal epithelia (Figure S2C,D) or ependymal cells of the adult brain (Figure S2E-G). However, a small but significant 1.13x increase in cilia length was noted in adult kidney cortical tubules (Figure S2H-J) and a 1.25x increase observed in liver bile ducts (Figure S2K-M). Lengthening of primary cilia in monociliated cells but not of cilia in multiciliated cells may be due to a dilution of ARL13B-Cerulean. Importantly, cilia lengthening as a result of ARL13B overexpression here, and in previous models, is tolerated *in vivo* and does not interfere with normal development as demonstrated by the grossly normal embryonic and adult phenotypes including; viability, growth and fertility observed in homozygous *R26Arl13b-Fucci2a*$^{Tg/Tg}$ animals (Figures S1F and S2). To our knowledge our Arl13b-Fucci2a reporter labels all cilia, as evidenced by sensitive detection of diverse cilia types found on neuronal, ependymal and choroid plexus cells in the adult brain (Figure S3).

Results:

Cilia persist after the G1/S transition in proliferating NIH 3T3 cells

It has been shown in cell synchronisation experiments that there are two distinct phases of cilia disassembly (Tucker, Pardee and Fujiwara, 1979; Pugacheva *et al.*, 2007). The first occurs 1-2 hours after serum stimulation, with the second occurring after 18-24 hours such that cells can re-enter the cell cycle. However, the precise timing of cilia assembly and disassembly in relation to the cell cycle in actively cycling cells is still unclear and has not been directly investigated by live imaging. In unsynchronised NIH 3T3 cells we frequently observed mVenus-hGem (1/110) positive cells (in S/G2/M) that harboured ARL13B-Cerulean labelled cilia (Figure 1B). To investigate this further, time-lapse imaging of cultured Arl13bCerulean-Fucci2a 3T3 cells was performed. We observed cilia assembly and disassembly and measured the timing of these events in parallel to Fucci2a cell cycle status and in relation to cytokinesis (Figure 2A-D). The

mean time for completion of cilia disassembly, as defined by complete loss of ARL13B-Cerulean localisation, was 65.50 ± 17.07 minutes prior to cytokinesis (Figure 2D). Often, loss of ARL13B-Cerulean localisation occurred immediately before (within the image acquisition time of 20 minutes per frame) the breakdown of the nuclear envelope (Movie S1 right panel). By defining the proportion of each cell cycle phase in which a cell was ciliated we were able to examine both the onset of ciliation and the point of resorption in detail (Figure 2C). To our surprise we observed cells initiating cilia formation at any point from early G1 through to mid S/G2/M with a mean (± 95 % CI) of 948.00 ± 140.62 minutes, whilst resorption was restricted close to cytokinesis (Figure 2C-D).

The propensity to ciliate and the timing of ciliation are both heterogeneous and heritable in NIH 3T3 cells

One cause of variation in ciliation time was the significantly faster ciliary assembly seen in daughter cells derived from a ciliated mother compared to those derived from non-ciliated mothers (Figure 2E). It is possible the intracellular metabolic environment inherited by daughter cells from a ciliated mother could prime them for early ciliogenesis. Reflecting this, a strong correlation was observed in the time taken for cilia assembly between sisters of a mitosis in the next cilia cycle (Figure 2F, Movie S1 right panel). Interestingly, although the timing of ciliary assembly between sisters was well correlated (Figure 2F), when the mean time taken for the first and second sisters to ciliate was compared a statistically significant difference was observed (Figure 2G). We hypothesise that this disparity reflects the proposed early formation of cilia in the sister that inherits the mother centriole (Anderson & Stearns, 2009; Paridaen et al., 2013). Taken together these data highlight that there is heterogeneity in the propensity to ciliate in NIH 3T3 cells and that this propensity is in part directly heritable.

The nuclear-ciliary angle correlates with directed movement in migrating NIH 3T3 cells

Primary cilia are known to be orientated between the nucleus and the leading edge during cell migration (Christensen et al., 2013; Schneider et al., 2010). It is not known whether this process

begins before cell migration or whether it is concomitant with cell movement. To understand how a cell may adopt this orientation, we performed time-lapse imaging of Arl13bCerulean-Fucci2a NIH 3T3 cells in a modified wound-healing assay (See Methods, Figure 3A-B, Movie S2). The angle between the primary cilium-to-nucleus and the nucleus-to-wound edge was determined five and ten hours after wound induction (Figure 3C-G) and compared to a control experiment where cells were seeded evenly onto a plate with no stimulus. We observed a homogeneous distribution of ciliary angles in the control group (Figure 3D). In response to the wound healing stimulus there was a significant reorientation of cilia perpendicular to the leading edge after 10 hours in culture (Figure 3E and F).

Scission of mature ciliary tips is required to stabilise cilia in NIH 3T3 cells

It has recently been shown that the tip of a primary cilium is actively severed in order to clear activated ciliary receptors (Nager *et al.*, 2017) and to initiate ciliary disassembly (Phua *et al.*, 2017). This scission process is mediated through an F-actin dependent mechanism (Nager *et al.*, 2017; Phua *et al.*, 2017) termed ectocytosis (Wood et al., 2013). In agreement with this proposed mechanism, mutants with compromised actin dynamics have delayed ciliary disassembly (Yeyati *et al.*, 2017). In these 'ectocytosis mutants', ciliogenesis is facilitated but ciliary stability is reduced resulting in an abnormally wide variation in ciliary lengths suggesting that actin-mediated ectocytosis plays a broader and constitutive role in the maintenance of cilia (Nager *et al.*, 2017; Yeyati *et al.*, 2017). To investigate this hypothesis we observed cilia growth during serum depletion in Arl13bCerulean-Fucci2a NIH 3T3 cells. By focusing on cells labelled with mCherry-hCdt1(30/120) (G1 phase only) we excluded ciliary ectocytosis events that would normally precede resorption during G2 phase prior to mitosis. In the absence of serum, we consistently found ciliary elongation after scission in G1 cilia (Figure 4A, Movie S3), confirming that ciliary scissions are not limited to cilia committed to resorb but can also occur under conditions that promote ciliary growth. We tested the dependence of G1-ectocytosis on actin dynamics through inhibition of the ARP2/3 complex activity, previously shown to participate in an F-actin ciliary gate

(Yeyati *et al.*, 2017). In control cultures, scission occurs mostly at the ciliary tip (38 cilia, 10/12 excisions occurring at tip), and was in some instances preceded by discernible ciliary swellings. Conversely, in the presence of the ARP2/3 inhibitor CK-666, cilia rapidly elongated, breaking frequently at the base and away from the tip (32 cilia, 4/16 excisions occurring at tip - Figure 4B and Movie S4) with bulges that often persisted throughout the time-lapse travelling repeatedly in anterograde or retrograde directions (Figure 4C, Movie S5). Morphometric comparisons confirmed that while control cilia present orderly growth and homogeneous morphology, CK-666 treated cilia changed shape rapidly and present a more disordered morphological profile (Figure 4D and E). The results further provide evidence that actin mediated trimming of the ciliary tip is operational all along the ciliary cycle and contributes to ciliary stability.

Arl13bCerulean-Fucci2a identifies the node as a cluster of ciliated cells in G1/G0

Left-right asymmetry is established in the early mouse embryo by the action of motile cilia in a specialised embryonic organiser structure known as the node located at the anterior end of the primitive streak (Lee and Anderson, 2008). The beating of these nodal cilia is required to generate nodal flow to break the left-right symmetry of the developing embryo (Nonaka *et al.*, 1998; McGrath *et al.*, 2003; Hirokawa *et al.*, 2006; Becker-Heck *et al.*, 2011; Shinohara *et al.*, 2012; Yoshiba *et al.*, 2012). This flow may be detected directly through a mechanosensory mechanism (Shinohara *et al.*, 2012) or may in turn generate a gradient of chemokines or chemokine containing ‘nodal vesicular particles’ (Tanaka, Okada and Hirokawa, 2005). Sensing of this gradient or flow may be achieved by specialised nonmotile cilia at the border or ‘crown’ of the node initiating asymmetric calcium signalling at its left margin (McGrath *et al.*, 2003).

We performed whole embryo live imaging of E7.5 *R26Arl13b-Fucci2aR*$^{+/Tg}$*; CAG-Cre*$^{+/Tg}$ embryos (n = 4, Downs and Davies stages: late streak (LS)- early headfold (EHF)) and were able to distinguish cell cycle stage specific abundance of the Fucci2a probes and localisation of ARL13B-Cerulean to primary cilia. As expected, our results revealed a clear demarcation in cell cycle status between the extraembryonic visceral endoderm and the embryonic visceral

endoderm and epiblast (distal) lineages (Figure 5A, Figure S4A-D). The majority of cells within the embryonic lineages were proliferating and therefore mVenus-hGem(1/110) positive.

However, as previously reported (Komatsu et al., 2011) the cells of the node were clearly identifiable as a cluster of mCherry-hCdt1(30/120) positive cells (in G1/G0) located at the tip of the embryo (Figure 5A-B, Figure S4A-F). Here, nodal cilia are orientated in what will become a 10µm deep concaved compartment, the nodal pit, discernible by ~E7.75 (Lee and Anderson, 2008). By turning the embryo and imaging directly into the node, approximately 180 nodal cilia labelled with ARL13B-Cerulean could be identified, consistent with previously reported numbers (200-300) (Shinohara *et al.*, 2012) (Figure S3G-I). We were unable to discriminate between pit and crown cilia at this stage as they do not become spatially distinct until slightly later. *R26Arl13b-Fucci2aR*$^{Tg/+}$ heterozygous mice therefore express the Arl13bCerulean-Fucci2a biosensor at levels high enough to enable high resolution live confocal imaging allowing discrimination of individual cells by cell cycle stage and the identification of cilia across lineages.

Arl13bCerulean-Fucci2a reports on primary cilia dynamics and cell cycle stage during organogenesis

To analyse cilia and cell cycle during organogenesis, we performed live imaging of whole-mount E8.5 embryos (n = 8, Downs and Davies stages: 0 somites (S)-8S stage) revealing the majority of cells to be ciliated, regardless of cell cycle stage (Figure 5C, Figure S5A-C). Very few cells within the prosencephalon were mCherry-hCdt1(30/120) positive at this stage, suggesting a high rate of proliferation (Figure S5A). Confocal sectioning revealed the lateral ventricles surrounded by an epithelium of highly proliferative cells, as shown by the high proportion of cells labelled with mVenus-hGem(1/110), orientated perpendicular to the lumen (Figure 5D and Figure S5D-I and Movie S6). The lumen of the lateral ventricles contained a high density of primary cilia projecting from the surrounding neuroprogenitor cells (Figure 5D, Figure S5G-I).

Within the E8.5 rhombencephalic region, the first somites were identifiable as morphologically distinct segmented groups of cells, predominantly in S/G2/M phases of the cell cycle (Figure 5E-

F, Figure S6). Cilia were clearly identifiable on cells surrounding the somites in G1 and S/G2/M stages of the cell cycle (Figure 5E-F, Figure S6A-C). Within each somite a high density of primary cilia were located projecting into the central core (Figure 5F, Figure S6D-F). The presence of primary cilia within both emerging and mature somites coincides with the induction of sclerotome development by SHH gradients (Fan and Tessier-Lavigne, 1994). *R26Arl13b-Fucci2aR* is the first model allowing simultaneous imaging of cilia and cell cycle progression during development. Our *in vivo* observations suggest that cilia persist through the G1/S transition and into S/G2/M phase during development in agreement with our observations in actively cycling NIH 3T3 cells in culture (Figure S7).

Live imaging of primary Arl13bCerulean-Fucci2a labelled cells captures cilia dynamics during differentiation and regeneration

To use our *R26Arl13b-Fucc2aR* mice as a tool to visualize the interplay between cilia types and cell cycle status during differentiation, we turned our attention to the emergence of motile cilia on differentiated cells. Multiciliated primary ependymal cultures were derived from the ventricular zone of E18.5 *R26Arl13b-Fucc2aR*$^{+/Tg}$*; CAG-Cre*$^{+/Tg}$ embryos. In early expanding cultures, ependymal cells were proliferative as demonstrated by the presence of cells in S/G2/M phases of the cell cycle, with ARL13B-Cerulean positive primary cilia identifiable on the majority of cycling cells (Figure 6A-C). Upon reaching confluency and serum starvation all cells entered G1/G0 labelled with mCherry-hCdt1(30/120). Upon differentiation (seven days after serum starvation), the absence of cycling mVenus-hGem(1/110) ependymal cells and the emergence of cells exhibiting multiple motile cilia (Figure 6D-I) was observed. High-speed confocal imaging confirmed the motility of these cilia, which moved in a periodic unidirectional whip-like motion required to generate cerebrospinal flow (Movie S7).

Cells of the adult hepatic ductal tree are largely quiescent with long monocilia (Figure S2K). These can be isolated to grow organoids which are genetically stable and can be passaged indefinitely, making them an attractive model for liver disease modelling. We derived hepatic ductal organoids and performed time-lapse imaging. In agreement with the data obtained from

Arl13bCerulean-Fucci2a NIH 3T3 cells, we observed many mVenus-hGem(1/110)+ cells simultaneously harbouring ARL13BCerulean+ cilia with rapid loss of cilia prior to mitosis and asymmetric rates of ciliation between daughters (Movie S8).

Endoderm restricted expression of Arl13bCerulean-Fucci2a reveals the luminal protrusion of primary cilia during lung branching morphogenesis

To demonstrate tissue-specific expression of Arl13bCerulean-Fucci2a in *R26Arl13b-Fucci2aR* mice, we crossed the reporter with endoderm specific *Sox17-2A-iCre* expressing mice. *Sox17-2A-iCre* mice were previously shown to label all endoderm derived tissues including the developing lung epithelium as well as the haematopoietic and vascular lineages (Engert et al., 2009). Live imaging of dissected E11.5 lungs after 12 hours of culture revealed restricted lung epithelial expression of Arl13bCerulean-Fucci2a as well as expression in a sub-population of migratory cells (Figure 7A-C) most likely of the haematopoietic, vasculature and smooth muscle lineages also derived from SOX17 expressing endoderm (Engert et al., 2009). Cells of the proximal lung epithelium were predominately labelled with mCherry-hCdt1(30/120) consistent with a population exiting the cell cycle and entering G0 (Figure 7A). In contrast, a high level of proliferation indicated by the high proportion of mVenus-hGem(1/110) positive cells was seen in actively branching apical tips of the epithelium (Figure 7G-I). This is in agreement with previous observations in cultured lungs from *R26Fucci2aR*$^{+/Tg}$*; CAG-Cre*$^{+/Tg}$ embryos (Mort *et al.*, 2014). Motile cilia in the mouse lung form from E14.5 (Rawlins et al., 2007), however primary cilia have been identified as early as E12.5 (Jain *et al.*, 2010). Using live imaging of E11.5 lung organotypic cultures, we were able to visualise primary cilia along the entire length of the lung epithelium within the actively branching regions at distal branch tips and within the more proximal airway epithelium where proliferation has ceased. Cilia were observed on the apical surface of the proximal and distal cells, orientated so that they project into the adjacent lumen (Figure 7D-F and G-I).

Discussion

Here we describe the design and validation of an Arl13bCerulean-Fucci2a tricistronic reporter construct encoding optimally spectrally separated biosensors that label both primary and motile cilia with ARL13B-Cerulean and report cell cycle progression through the Fucci2a cell cycle probes (Abe *et al.*, 2013; Mort *et al.*, 2014).

Unearthing unexplored ciliary parameters

In previous reports the preference of cells to orientate their primary cilia towards the leading edge during migration and in response to chemoattractant cues was observed but the timing not determined (Schneider *et al.*, 2010; Christensen *et al.*, 2013; McGowan and McCoy, 2013). Our results suggest that this reorientation is in part due to the cytoskeletal changes required for directed migration and does not require the presence of a chemoattractant. As well as investigating cilia orientation, Arl13bCerulean-Fucci2a offers the means to easily separate other ciliary events, such as scission, according to cell cycle phase. We propose that ciliary scission does not just precede ciliary resorption but is instead required throughout the ciliary cycle to maintain ciliary length within its normal range. Scission may coordinate the growth rate of the ciliary membrane with that of the axoneme and the uncoupling of these events may destabilise cilia.

Persistence of cilia after the G1/S transition is a general property in cells and mice

Previous studies have used serum starvation to synchronise NIH 3T3 or retinal pigment epithelial (RPE1) cells in G1 followed by serum addition to drive cilia disassembly. These studies reported cilia reassembly in G1 and two rounds of cilia disassembly, 1-2 hours and 18-24 hours after the addition of serum. The second round of disassembly occurring around the time of DNA replication (Tucker, Pardee and Fujiwara, 1979; Pugacheva *et al.*, 2007; Spalluto, Wilson and Hearn, 2013). We show here, that cilia generally assemble during G1 and that the completion of cilia disassembly is close to cytokinesis, often within 20 minutes of the breaking of the nuclear envelope at mitosis. This is consistent with previous reports in rat kangaroo kidney epithelial

(PtK1) cells showing disassembly in early M-phase (Rieder et al., 1979). The strength of our model is that we can resolve individual cells in physiologically relevant unsynchronised cell populations rather than by using artificial synchronisation protocols.

A popular school of thought is that the primary cilium is resorbed or shed at the G1-S transition such that centriole duplication can then proceed (Hinchcliffe and Sluder, 2001; Nigg and Stearns, 2011). However, our data suggests that the presence of a primary cilium and the duplication of the centrioles are not mutually exclusive in NIH 3T3 cells. But rather that the mother centriole is acting as the basal body of the cilia whilst centriole duplication is occurring. Primary cilia were also identified on cells in G1 and S/G2/M stages in all examined tissues in the developing mouse (Figure S7), suggesting that this is a common mechanism. Persistence of cilia into late S/G2/M-phase may result in sequestering of one set of centrioles at the base of the cilia prior to mitotic spindle formation, influencing the future plane of cell division. Interestingly, kidney specific deletion of *Ift20* and *Kif3a* misorientates spindle assembly concurrent with cilia loss resulting in epithelial cyst formation and suggesting a potential role of cilia in the positioning of the mitotic spindle (Jonassen *et al.*, 2008; Patel *et al.*, 2008). Many cilia and centriole associated proteins have cilia-independent functions essential for correct spindle formation and cytokinesis (Vertii *et al.*, 2015). Therefore, careful dissection of cilia-dependent and independent functions is required to determine the importance of primary cilia in spindle orientation.

Tracking ciliary assembly and disassembly and the heritability of a primed ciliary state

Our data supports previous reports that the mother centriole can prime a cell to ciliate (Anderson and Stearns, 2009). This phenomenon may determine fate choice decisions in embryonic neocortical stem cells during neurogenesis (Paridaen et al., 2013). The inheritance of the mother centriole in neocortical progenitors, identified by the association with remnants of the ARL13B^{+} cilia membrane, enabled one daughter to reassemble its primary cilia faster and asymmetrically retain its position in the stem cell niche while the second daughter is destined for differentiation.

The ARL13B-Cerulean model now provides a tool to assess whether this might be a common mechanism in asymmetric cell fate decisions *in vitro* and *in vivo*.

A new mouse reporter for combined live imaging of ciliogenesis and the cell cycle

In agreement with previous studies we could clearly distinguish the embryonic node at E7.5 as a collection of mCherry-hCdt1(30/120) positive cells harbouring ARL13B-Cerulean labelled cilia at the anterior tip of embryo (Komatsu et al., 2011). In the E8.5 prosencephalon, neuroepithelial cells surrounding the lateral ventricles projected their primary cilia into the luminal space reminiscent of the orientation of primary cilia during neurogenesis (Paridaen et al., 2013). This developmental stage precedes neurogenesis, which commences around E11; here the neuroepithelium surrounding the ventricles is constructed of a single layer of neural stem cells organised into a pseudostratified neuroepithelium (Götz and Huttner, 2005). It has been shown that during neurogenesis the cerebrospinal fluid (CSF) provides proliferative and survival support to neural progenitors by IGF2 signalling with binding enriched along primary cilia (Lehtinen *et al.*, 2011). It is possible the anchoring of cells to the ventricular lumen via a ciliated membrane at E8.5, prior to neurogenesis, may also be required to detect signals in the CSF necessary to maintain their multipotent potential and promote proliferation.

SHH released from the notocord and floor plate has previously been shown to be necessary for somitogenesis by promoting proliferation and expression of the sclerotomal markers PAX1, PAX9 and SOX9 via the activity of the SHH signalling GLI transcription factors (Buttitta et al., 2003; Chiang et al., 1996; Fan & Tessier-Lavigne, 1994; Fan et al., 1995; Murtaugh et al., 1999; Zeng et al., 2002). Our identification of a high density of primary cilia within the developing somites suggests these cells are competent to receive and interpret the SHH signals required for their growth and differentiation.

Potential roles for ciliation in lung branching morphogenesis

Primary cilia have been identified on the luminal surface of E12.5 proximal lung epithelial cells

prior to the appearance of multiple motile cilia from E15.5 on post-mitotic airway epithelial cells (Jain *et al.*, 2010). Here we report the presence of primary cilia along the entire length of the luminal aspect of the lung epithelium during branching morphogenesis in cultured E11.5 lungs, including the most distal, actively branching and highly proliferative regions. The role of primary cilia during branching morphogenesis in the lung has not been addressed. However in the mammary gland disruption of ciliogenesis in double *Kif3a*/*Ift20* mutants results in severe branching defects in addition to increased canonical WNT and decreased SHH signalling (McDermott et al., 2010). An intriguing question is whether primary cilia have a similarly important role during lung epithelial branching. In the lung, SHH expression in the distal epithelium attenuates FGF10 released from the surrounding mesenchyme and is required for branch formation (Bellusci *et al.*, 1997; Warburton *et al.*, 2005). It is possible that sequestration of primary cilia to the luminal surface prevents autocrine cilia dependent signalling. Another intriguing role for primary cilia during lung branching morphogenesis could be in the establishment of epithelial planar cell polarity (PCP). It has been reported that the intraflagellar transport protein *Ift88* (essential for primary cilia assembly) is required for establishing PCP for convergent extension during mouse cochlear development (Jones *et al.*, 2008), suggesting a potential link between primary cilia and PCP, a process important for epithelial fold formation. In the lung, mice harbouring mutations in the PCP genes *Celsr1* or *Vangl2* exhibit reduced and misshapen branching (Yates *et al.*, 2010). It would be interesting to evaluate the potential role of lung epithelial primary cilia during branching morphogenesis by conditional deletion of cilia in the lung epithelium.

Limitations

R26Arl13b-Fucci2aR mice are the best available model for tracking the cell and cilia cycles with live imaging, however there are several limitations of the technology. First, because only the nuclei and the ciliary membrane are labelled it can be hard, especially in densely labelled static images, to correlate each cilium to a cell body. This could be circumvented in live tissues by

applying an appropriately chosen vital dye that preferentially labels the plasma membrane such as wheat germ agglutinin (Fu *et al.*, 2013), or by inducing expression in only a subset of cells using a CreERT2 expressing mouse line and titrating the tamoxifen dose. Second, although in all cells and tissues examined ARL13B-Cerulean appeared a ubiquitous marker of primary and motile cilia, we cannot rule out the existence of ARL13B-negative cilia where ARL13B-Cerulean does not localise correctly. Third, although there appears to be no gross phenotypic effect on the development, health or reproduction of homozygous Arl13b-Fucci2a – expressing animals, we cannot rule out subtle changes in cilia-based signalling due to ARL13B overexpression. To circumvent this, it may be possible to directly genome edit the *R26Arl13b-Fucci2aR* reporter mice to carry either of two mutations in the GTPase domain of ARL13B-Cerulean, T35N and R78Q, which localise to cilia without affecting length when over-expressed (Lu *et al.*, 2015).

Conclusion

We show here that persistence of cilia after the G1/S transition is a general property in proliferative cell populations. The *R26Arl13b-Fucci2aR* reporter mouse uniquely allows inducible, cell type specific expression of the Arl13bCerulean-Fucci2a biosensor, labelling both primary and motile cilia. The tricistronic nature of the *R26Arl13b-Fucci2aR* reporter mouse will allow researchers to reduce, refine and replace animals in their future research strategies by simplifying their genetic crosses and keeping fewer animals on the shelf. Tissue restricted expression should prove particularly useful in developmental studies where lineage tracing is required and where it may be important to distinguish between cycling and non-cycling cells within a ciliated population.

Acknowledgements:

The authors are grateful to: Joe Mee and the Scottish Center for Regenerative Medicine Transgenic Service for ES cell targeting; Fiona Kilanowski and Julia Dorin for ES cell karyotyping; the IGMM Advanced Imaging Resource for imaging support and Elisabeth Freyer for help and advice on FACS analysis. The work was supported by core funding from the Medical

Research Council (MC_PC_U127527200 to MJF, MAK, IJJ and RLM; MC_UU_12018/26 to PLY, GRM, SHW, EAH, PM; MC_PC_U127574433 to RRM. and HKM) and to RLM and IJJ by the NC3Rs (#NC/M001091/1).

Author contributions:

IJJ, PM and RLM conceived the study, MJF, PM and RLM prepared the manuscript. RLM made the ES cell targeting construct and screened the ES cells. ATD made the Flp/In targeting construct. GM assisted with primary ependymal cultures. SHW and LB isolated, imaged and analysed adult liver studies. MJF, PLY, and PM performed cell culture and image analysis experiments and imaged mouse tissues. MAK maintained the mouse colonies. HKM and RRM assisted with ES cell culture and imaging. ASS and MA provided the Fucci2 constructs and commented on the manuscript. EAH cloned *Arl13b* and commented on the manuscript.

Declaration of interests:

The authors declare no competing interests.

References:

Abe, T. *et al.* (2013) 'Visualization of cell cycle in mouse embryos with Fucci2 reporter directed by Rosa26 promoter.', *Development (Cambridge, England)*, 140(1), pp. 237–46. doi: 10.1242/dev.084111.

Anderson, C. T. and Stearns, T. (2009) 'Centriole Age Underlies Asynchronous Primary Cilium Growth in Mammalian Cells', *Current Biology*. Elsevier Ltd, 19(17), pp. 1498–1502. doi: 10.1016/j.cub.2009.07.034.

Bangs, F. K. *et al.* (2015) 'Lineage specificity of primary cilia in the mouse embryo', 17(2), pp. 113–122. doi: 10.1038/ncb3091.Lineage.

Becker-Heck, A. *et al.* (2011) 'The coiled-coil domain containing protein CCDC40 is essential for motile cilia function and left-right axis formation', *Nat Genet*. Nature Publishing Group, a division of Macmillan Publishers Limited. All Rights Reserved., 43(1), pp. 79–84.

Bellusci, S. *et al.* (1997) 'Involvement of Sonic hedgehog (Shh) in mouse embryonic lung growth and morphogenesis', *Development*, 124, pp. 53–63.

Borovina, A. *et al.* (2010) 'Vangl2 directs the posterior tilting and asymmetric localization of motile primary cilia', *Nature Cell Biology*. Nature Publishing Group, 12(4), pp. 407–412. doi: 10.1038/ncb2042.

Buttitta, L. *et al.* (2003) 'Interplays of Gli2 and Gli3 and their requirement in mediating Shh- dependent sclerotome induction', *Development*, 130, pp. 6233–6243.

Cantagrel, V. *et al.* (2008) 'Mutations in the Cilia Gene ARL13B Lead to the Classical Form of Joubert Syndrome', *The American Journal of Human Genetics*, 83(2), pp. 170–179. doi: 10.1016/j.ajhg.2008.06.023.

Caspary, T., Larkins, C. E. and Anderson, K. V. (2007) 'The Graded Response to Sonic Hedgehog Depends on Cilia Architecture', *Developmental Cell*, 12(5), pp. 767–778. doi: 10.1016/j.devcel.2007.03.004.

Chiang, C. *et al.* (1996) 'Cyclopia and defective axial patterning in mice lacking Sonic hedgehog gene

function.', *Nature*, pp. 407–413. doi: 10.1038/383407a0.

Christensen, S. T. *et al.* (2013) 'Analysis of primary cilia in directional cell migration in fibroblasts', *Methods in Enzymology*, 525, pp. 45–58. doi: 10.1016/B978-0-12-397944-5.00003-1.

Delling, M. *et al.* (2013) 'Primary cilia are specialized calcium signalling organelles', *Nature*. Nature Publishing Group, 504(7479), pp. 311–314. doi: 10.1038/nature12833.

Engert, S. *et al.* (2009) 'Sox17-2A-iCre: a knock-in mouse line expressing Cre recombinase in endoderm and vascular endothelial cells.', *Genesis (New York, N.Y. : 2000)*, 47(9), pp. 603–10. doi: 10.1002/dvg.20540.

Fan, C.-M. and Tessier-Lavigne, M. (1994) 'Patterning of mammalian somites by surface ectoderm and notochord: Evidence for sclerotome induction by a hedgehog homolog', *Cell*, 79(7), pp. 1175–1186. doi: http://dx.doi.org/10.1016/0092-8674(94)90009-4.

Fan, C. M. *et al.* (1995) 'Long-range sclerotome induction by sonic hedgehog: Direct role of the amino-terminal cleavage product and modulation by the cyclic AMP signaling pathway', *Cell*, 81(3), pp. 457–465. doi: 10.1016/0092-8674(95)90398-4.

Fu, Y.-Y. *et al.* (2013) '3-D imaging and illustration of mouse intestinal neurovascular complex', *American Journal of Physiology-Gastrointestinal and Liver Physiology*, 304(1), pp. G1–G11. doi: 10.1152/ajpgi.00209.2012.

Goetz, S. C. and Anderson, K. V (2010) 'The primary cilium: a signalling centre during vertebrate development.', *Nature reviews. Genetics*. Nature Publishing Group, 11(5), pp. 331–44. doi: 10.1038/nrg2774.

Götz, M. and Huttner, W. B. (2005) 'The cell biology of neurogenesis', *Nat Rev Mol Cell Biol*, 6(10), pp. 777–788. doi: 10.1038/nrm1739.

Han, Y. *et al.* (2009) 'Dual and opposing roles of primary cilia in medulloblastoma development', *Nat Med*, 15(9), pp. 1062–1065. doi: 10.1038/nm.2020.Dual.

Hassounah, N. B. *et al.* (2013) 'Primary Cilia Are Lost in Preinvasive and Invasive Prostate Cancer', *PLoS ONE*, 8(7), pp. 1–19. doi: 10.1371/journal.pone.0068521.

Hinchcliffe, E. H. and Sluder, G. (2001) '"It takes two to tango": Understanding how centrosome duplication is regulated throughout the cell cycle', *Genes and Development*, pp. 1167–1181. doi: 10.1101/gad.894001.

Hirokawa, N. *et al.* (2006) 'Nodal Flow and the Generation of Left-Right Asymmetry', *Cell*, 125(1), pp. 33–45. doi: 10.1016/j.cell.2006.03.002.

Hohenstein, P. *et al.* (2008) 'High-efficiency Rosa26 knock-in vector construction for Cre-regulated overexpression and RNAi', *PathoGenetics*, 1, p. 3. doi: 10.1186/1755-8417-1-3.

Izawa, I. *et al.* (2015) 'Current topics of functional links between primary cilia and cell cycle.', *Cilia*. BioMed Central, 4, p. 12. doi: 10.1186/s13630-015-0021-1.

Jain, R. *et al.* (2010) 'Temporal relationship between primary and motile ciliogenesis in airway epithelial cells', *American Journal of Respiratory Cell and Molecular Biology*, 43(6), pp. 731–739. doi: 10.1165/rcmb.2009-0328OC.

Jonassen, J. A. *et al.* (2008) 'Deletion of IFT20 in the mouse kidney causes misorientation of the mitotic spindle and cystic kidney disease', *Journal of Cell Biology*, pp. 377–384. doi: 10.1083/jcb.200808137.

Jones, C. *et al.* (2008) 'Ciliary proteins link basal body polarization to planar cell polarity regulation.', *Nature genetics*, 40(1), pp. 69–77. doi: 10.1038/ng.2007.54.

Komatsu, Y., Kaartinen, V. and Mishina, Y. (2011) 'Cell cycle arrest in node cells governs ciliogenesis at the node to break left-right symmetry.', *Development (Cambridge, England)*, 138(August), pp. 3915–3920. doi: 10.1242/dev.073650.

Larkins, C. E. *et al.* (2011) 'Arl13b regulates ciliogenesis and the dynamic localization of Shh signaling proteins.', *Molecular biology of the cell*. American Society for Cell Biology, 22(23), pp. 4694–703. doi: 10.1091/mbc.E10-12-0994.

Lee, J. D. and Anderson, K. V. (2008) 'Morphogenesis of the node and notochord: The cellular basis for the establishment and maintenance of left-right asymmetry in the mouse', *Developmental Dynamics*, 237(12), pp. 3464–3476. doi: 10.1002/dvdy.21598.

Lehtinen, M. K. *et al.* (2011) 'The Cerebrospinal Fluid Provides a Proliferative Niche for Neural Progenitor Cells', *Neuron*. Elsevier Inc., 69(5), pp. 893–905. doi: 10.1016/j.neuron.2011.01.023.

Lin, F. *et al.* (2003) 'Kidney-specific inactivation of the KIF3A subunit of kinesin-II inhibits renal ciliogenesis and produces polycystic kidney disease.', *Proceedings of the National Academy of Sciences of the United States of America*, 100(9), pp. 5286–91. doi: 10.1073/pnas.0836980100.

Lu, H. *et al.* (2015) 'A function for the Joubert syndrome protein Arl13b in ciliary membrane extension and ciliary length regulation', *Developmental Biology*. Academic Press, 397(2), pp. 225–236. doi: 10.1016/J.YDBIO.2014.11.009.

Ma, M. *et al.* (2013) 'Loss of cilia suppresses cyst growth in genetic models of autosomal dominant polycystic kidney disease.', *Nature genetics*, 45(9), pp. 1004–12. doi: 10.1038/ng.2715.

Maskey, D. *et al.* (2015) 'Cell cycle-dependent ubiquitylation and destruction of NDE 1 by CDK 5 - FBW 7 regulates ciliary length', *The EMBO journal*, 34(19), pp. 1–17.

McDermott, K. M. *et al.* (2010) 'Primary cilia regulate branching morphogenesis during mammary gland development.', *Current biology : CB*, 20(8), pp. 731–7. doi: 10.1016/j.cub.2010.02.048.

McGowan, S. E. and McCoy, D. M. (2013) 'Platelet-derived growth factor-A and sonic hedgehog signaling direct lung fibroblast precursors during alveolar septal formation.', *American journal of physiology. Lung cellular and molecular physiology*, 305(3), pp. L229-39. doi: 10.1152/ajplung.00011.2013.

McGrath, J. *et al.* (2003) 'Two populations of node monocilia initiate left-right asymmetry in the mouse.', *Cell*, 114(1), pp. 61–73. Available at: http://www.ncbi.nlm.nih.gov/pubmed/12859898 (Accessed: 7 June 2018).

Menzl, I. *et al.* (2014) 'Loss of primary cilia occurs early in breast cancer development.', *Cilia*, 3(7), pp. 1–16. doi: 10.1186/2046-2530-3-7.

Miyazaki, J. *et al.* (1989) 'Expression vector system based on the chicken β-actin promoter directs efficient production of interleukin-5', *Gene*, 79(2), pp. 269–277. doi: 10.1016/0378-1119(89)90209-6.

Mort, R. L. *et al.* (2014) 'Fucci2a: A bicistronic cell cycle reporter that allows Cre mediated tissue

specific expression in mice', *Cell Cycle*, 13(17). doi: 10.4161/15384101.2015.945381.

Mort, R. L., Hay, L. and Jackson, I. J. (2010) 'Ex vivo live imaging of melanoblast migration in embryonic mouse skin', *Pigment Cell and Melanoma Research*, 23(2). doi: 10.1111/j.1755-148X.2010.00669.x.

Murtaugh, L. C., Chyung, J. H. and Lassar, A. B. (1999) 'Sonic hedgehog promotes somitic chondrogenesis by altering the cellular response to BMP signaling', *Genes and Development*, 13(2), pp. 225–237. doi: 10.1101/gad.13.2.225.

Nager, A. R. *et al.* (2017) 'An Actin Network Dispatches Ciliary GPCRs into Extracellular Vesicles to Modulate Signaling', *Cell*. Elsevier, 168(1), p. 252–263.e14. doi: 10.1016/j.cell.2016.11.036.

Nigg, E. A. and Stearns, T. (2011) 'The centrosome cycle: Centriole biogenesis, duplication and inherent asymmetries', *Nature Cell Biology*. Nature Publishing Group, 13(10), pp. 1154–1160. doi: 10.1038/ncb2345.

Nonaka, S. *et al.* (1998) 'Randomization of left-right asymmetry due to loss of nodal cilia generating leftward flow of extraembryonic fluid in mice lacking KIF3B motor protein', *Cell*, 95(6), pp. 829–837. doi: 10.1016/S0092-8674(00)81705-5.

Paridaen, J. T. M. L., Wilsch-Bräuninger, M. and Huttner, W. B. (2013) 'Asymmetric inheritance of centrosome-associated primary cilium membrane directs ciliogenesis after cell division', *Cell*, 155(2), pp. 333–344. doi: 10.1016/j.cell.2013.08.060.

Patel, V. *et al.* (2008) 'Acute kidney injury and aberrant planar cell polarity induce cyst formation in mice lacking renal cilia', *Human Molecular Genetics*, 17(11), pp. 1578–1590. doi: 10.1093/hmg/ddn045.

Phua, S. C. *et al.* (2017) 'Dynamic Remodeling of Membrane Composition Drives Cell Cycle through Primary Cilia Excision', *Cell*. Elsevier, 168(1–2), p. 264–279.e15. doi: 10.1016/j.cell.2016.12.032.

Pintado, P. *et al.* (2015) 'Arl13b interferes with α-tubulin acetylation', *Cilia*. BioMed Central, 4(Suppl 1), p. P73. doi: 10.1186/2046-2530-4-S1-P73.

Pugacheva, E. N. *et al.* (2007) 'HEF1-Dependent Aurora A Activation Induces Disassembly of the

Primary Cilium', *Cell*, 129(7), pp. 1351–1363. doi: 10.1016/j.cell.2007.04.035.

Rawlins, E. L. *et al.* (2007) 'Lung development and repair: contribution of the ciliated lineage.', *Proceedings of the National Academy of Sciences of the United States of America*, 104(2), pp. 410–417. doi: 10.1073/pnas.0610770104.

Reiter, J. F. and Leroux, M. R. (2017) 'Genes and molecular pathways underpinning ciliopathies', *Nature Reviews Molecular Cell Biology*. Nature Publishing Group, 18(9), pp. 533–547. doi: 10.1038/nrm.2017.60.

Rieder, C. L., Jensen, C. G. and Jensen, L. C. W. (1979) 'The resorption of primary cilia during mitosis in a vertebrate (PtK1) cell line', *Journal of Ultrastructure Research*. Academic Press, 68(2), pp. 173–185. doi: 10.1016/S0022-5320(79)90152-7.

Rizzo, M. a *et al.* (2004) 'An improved cyan fluorescent protein variant useful for FRET.', *Nature biotechnology*, 22(4), pp. 445–449. doi: 10.1038/nbt945.

Sakaue-Sawano, A. *et al.* (2008) 'Visualizing spatiotemporal dynamics of multicellular cell-cycle progression.', *Cell*, 132(3), pp. 487–98. doi: 10.1016/j.cell.2007.12.033.

Schmitz, F. *et al.* (2017) 'A novel Cre-inducible knock-in ARL13B-tRFP fusion cilium reporter', *genesis*, 55(11), p. e23073. doi: 10.1002/dvg.23073.

Schneider, C. A., Rasband, W. S. and Eliceiri, K. W. (2012) 'NIH Image to ImageJ: 25 years of image analysis', *Nature Methods*. Nature Publishing Group, 9(7), pp. 671–675. doi: 10.1038/nmeth.2089.

Schneider, L. *et al.* (2010) 'Directional Cell Migration and Chemotaxis in Wound Healing Response to PDGF-AA are Coordinated by the Primary Cilium in Fibroblasts', *Cellular Physiology and Biochemisty*, (25), pp. 279–292.

Seeley, E. S. and Nachury, M. V (2010) 'The perennial organelle: assembly and disassembly of the primary cilium.', *Journal of cell science*, 123(Pt 4), pp. 511–8. doi: 10.1242/jcs.061093.

Shaner, N. C., Steinbach, P. A. and Tsien, R. Y. (2005) 'A guide to choosing fluorescent proteins.', *Nature methods*, 2(12), pp. 905–909. doi: 10.1038/nmeth819.

Shinohara, K. *et al.* (2012) 'Two rotating cilia in the node cavity are sufficient to break left–right symmetry in the mouse embryo', *Nature Communications*, 3, p. 622. doi: 10.1038/ncomms1624.

Soriano, P. (1999) 'Generalized lacZ expression with the ROSA26 Cre reporter strain.', *Nature genetics*, 21(1), pp. 70–71. doi: 10.1038/5007.

Spalluto, C., Wilson, D. I. and Hearn, T. (2013) 'Evidence for reciliation of RPE1 cells in late G1 phase, and ciliary localisation of cyclin B1', *FEBS Open Bio*. Elsevier Ltd., 3, pp. 334–340. doi: 10.1016/j.fob.2013.08.002.

Strathdee, D., Ibbotson, H. and Grant, S. G. N. (2006) 'Expression of transgenes targeted to the Gt(ROSA)26Sor locus is orientation dependent.', *PloS one*, 1(1), p. e4. doi: 10.1371/journal.pone.0000004.

Tanaka, Y., Okada, Y. and Hirokawa, N. (2005) 'FGF-induced vesicular release of Sonic hedgehog and retinoic acid in leftward nodal flow is critical for left–right determination', *Nature*, 435(7039), pp. 172–177. doi: 10.1038/nature03494.

Tucker, R. W., Pardee, A. B. and Fujiwara, K. (1979) 'Centriole ciliation is related to quiescence and DNA synthesis in 3T3 cells', *Cell*, 17(3), pp. 527–535. doi: 10.1016/0092-8674(79)90261-7.

Vertii, A. *et al.* (2015) 'New frontiers: discovering cilia-independent functions of cilia proteins', *EMBO reports*, 16(10), pp. 1275–1287. doi: 10.15252/embr.201540632.

Wang, W., Wu, T. and Kirschner, M. W. (2014) 'The master cell cycle regulator APC-Cdc20 regulates ciliary length and disassembly of the primary cilium', *eLife*, 3, p. e03083. doi: 10.7554/eLife.03083.

Warburton-Pitt, S. R. F. *et al.* (2014) 'The nphp-2 and arl-13 Genetic Modules Interact to Regulate Ciliogenesis and Ciliary Microtubule Patterning in C. elegans', *PLoS Genetics*. Edited by S. K. Dutcher. Public Library of Science, 10(12), p. e1004866. doi: 10.1371/journal.pgen.1004866.

Warburton, D. *et al.* (2005) 'Molecular mechanisms of early lung specification and branching morphogenesis.', *Pediatric research*, 57(5 Pt 2), p. 26R–37R. doi: 10.1203/01.PDR.0000159570.01327.ED.

Wong, S. Y. *et al.* (2009) 'Primary cilia can both mediate and suppress Hedgehog pathway-dependent

tumorigenesis', *Nat Med*, 15(9), pp. 1055–1061. doi: 10.1038/nm.2011.Primary.

Wood, C. R. *et al.* (2013) 'The cilium secretes bioactive ectosomes', *Current Biology*. Elsevier Ltd, 23(10), pp. 906–911. doi: 10.1016/j.cub.2013.04.019.

Yates, L. L. *et al.* (2010) 'The PCP genes Celsr1 and Vangl2 are required for normal lung branching morphogenesis', *Human Molecular Genetics*, 19(11), pp. 2251–2267. doi: 10.1093/hmg/ddq104.

Yeyati, P. L. *et al.* (2017) 'KDM3A coordinates actin dynamics with intraflagellar transport to regulate cilia stability', *The Journal of cell biology*, 216(4), pp. 999–1013. doi: 10.1083/jcb.201607032.

Ying, Q.-L. *et al.* (2008) 'The ground state of embryonic stem cell self-renewal', *Nature*, 453(7194), pp. 519–523. doi: 10.1038/nature06968.

Yoshiba, S. *et al.* (2012) 'Cilia at the node of mouse embryos sense fluid flow for left-right determination via Pkd2', *Science*, 338(6104), pp. 226–231. doi: 10.1016/j.cmet.2012.08.002.

Zeng, L. *et al.* (2002) 'Shh establishes an Nkx3.2/Sox9 autoregulatory loop that is maintained by BMP signals to induce somitic chondrogenesis', *Genes and Development*, 16(15), pp. 1990–2005. doi: 10.1101/gad.1008002.

Figure Legends:

Figure 1: Design and characterisation of an Arl13bCerulean-Fucci2a reporter with stable integration and expression in an NIH 3T3 cell line: (A) The full length mouse *Arl13b* cDNA was fused to mCerulean and combined with the Fucci2a probes mCherry-hCdt1(30/120) and mVenus-hGem(1/110) separated by the self-cleaving peptides P2A and T2A respectively. Expression of this tricistronic construct is driven by the CAG promoter. A stable NIH 3T3 cell line was generated using the Flp-In system incorporating a single copy of Arl13bCerulean-Fucci2a by co-transfection of pCDNA5-CAG-Arl13bCerulean-Fucci2a and the Flp-recombinase expressing plasmid pOG44. **(B)** Live confocal images of the Arl13bCerulean-Fucci2a 3T3 cells showing nuclei distributed throughout the G1 or S/G2M cell cycle phases and labelled with mCherry-hCdt1(30/120) or mVenus-hGem(1/110) respectively. Single primary cilia are apparent on cells in both G1 and S/G2/M phases of the cell cycle (arrows in B - inset). **(C-D)** FACS analysis of

Arl13bCerulean-Fucci2a 3T3 cells showed distinct mCherry-hCdt1(30/120) and mVenus-hGem(1/110) labelled cell populations **(D)** when compared to a control cell line **(C). (E)** DAPI staining and FACS analysis to determine the DNA content of the mCherry-hCdt1(30/120) and mVenus-hGem(1/110) populations in **(C)** confirmed faithful reporting of cell cycle stage; mCherry-hCdt1(30/120) positive cells exhibit a classical 2n peak confirming they are in the G1 cell cycle phase; mVenus-hGem (1/110) positive cells exhibit a long peak between 2n and 4n confirming a population of cells in S, G2 and M phases of the cell cycle. Scale bar in B = 100 μm, scale bar in B (inset) = 50 μm.

Figure 2: The dynamics of the cilia assembly and disassembly cycle in Arl13bCerulean-Fucci2a NIH 3T3 cells: (A) Cell cycle progression of a single Arl13bCerulean-Fucci2a labelled nucleus as it cycles from G1 through S and G2 phases and undergoes mitosis. The sequential peaks of mCherry-hCdt1(30/120) and mVenus-hGem(1/110) are evident as is the presence of a single Arl13b-Cerulean labelled cilia during the G1, S and G2 phases before being disassembled shortly before mitosis. **(B)** The dynamics of the cilia cycle in Arl13bCerulean-Fucci2a 3T3 cells were determined in time-lapse experiments. We defined cilia assembly and disassembly times as the time between cytokinesis and the initiation of cilia formation or the completion of cilia resorption (loss of ARL13B-Cerulean localisation). **(C)** Analysis of individual cell ciliation events showing the ciliation state of each cell and its relative position within the G1 and S/G2/M cell cycle phases (n = 40 ciliation events). **(D)** Analysis of cilia assembly and disassembly times in cycling Arl13bCerulean-Fucci2a 3T3 cells (n = 40) revealed that while cilia assembly time varied greatly, disassembly happens in a relatively tight window. **(E)** We compared the behaviour of the progeny of ciliated and non-ciliated cells. Cilia assembly is significantly faster after mitosis in the progeny of ciliated mother cells compared to the progeny of non-ciliated mothers (Students t-test $P < 0.001$, n = 20 in each group). **(F)** Further investigation of the variation in cilia assembly time revealed a positive correlation between the cilia assembly times of the direct daughters of a mitosis (Spearman's Rank $P < 0.01$, $r = 0.7$, n = 12 pairs) but not between randomly paired cells (Spearman's Rank $P > 0.05$, $r = -0.2$, n = 12 pairs). **(G)** Comparing the sisters in individual

daughter pairs revealed that one daughter typically lagged behind the other in the time taken to initiate cilia formation, we termed these daughters leading and lagging cells. There is a significant difference in cilia assembly timing between these groups (Students t-test $P < 0.001$, n = 37 daughter pairs). Boxplots indicate; min, max, median and interquartile range, all values are shown. Scale bar in A = 10 μm, t = time in hours.

Figure 3: Arl13bCerulean-Fucci2a 3T3 cells orientate their cilia towards the leading edge concurrent to migration during wound healing: (A-B) Images taken of Arl13bCerulean-Fucci2a 3T3 cells migrating into the cell free space after the removal of a silicon barrier and after 10 hours of wound healing. **(C)** The orientation of the primary cilium was calculated for individual cells by measuring the angle between the centre of the cell's nucleus and the cilium followed by normalisation to the collective angle of migration. **(D)** A histogram of ciliary angles in a control experiment in which there is no directional movement shows a uniform distribution of ciliary angles (n = 387 cilia). **(E-F)** In the migration assay 5 and 10 hours after removal of the silicon barrier the majority of cells have reoriented their primary cilia so that the distribution of angles coalesces around the direction of migration (n = 133 and 135 cilia respectively). After 10 hours the distribution of cilia angles was shown to differ significantly from the uniform distribution observed in the control experiment (two sample Kolmogorov-Smirnov test $P < 0.05$). Scale bar in A-B = 50 μm.

Figure 4: Ciliary decapitation occurs during ciliary growth in G1 and is dependent on F-actin. (A) Live imaging of Arl13bCerulean-Fucci2a NIH 3T3 cells in G1 (mCherry-hCdt1(30/120) positive) showing cilia decapitation (arrows at 17 and 40 mins) prior to cilia elongation. **(B)** The addition of 200μM F-actin inhibitor (CK-666) destabilised cilia resulting in frequent decapitations (arrow at 40 mins) far from the scission point. **(C)** Cilia swellings moving in the anterograde direction (F) were occasionally observed prior to cilia scission. In the presence of CK-666 swellings were observed moving in both anterograde (F) and retrograde (R) directions. **(D)** The bounding box (BBox – minimum bounding rectangular cuboid) of each cilium was identified using image processing and a comparison of the BBox morphology of elongating cilia after serum

starvation was performed. Cilia assembling in the presence of CK-666 are less stable and have a deformed morphology compared to controls. **(E)** Scatterplot correlating the bounding box length and volume of elongating cilia at the start and end of the time lapse experiment in (D). Comparison of the ratio of Volume:Length showed a statistically significant difference between the control and CK-666 treated groups at 120 minutes (2-Way ANOVA $P < 0.0001$, Tukey's HSD $P < 0.0001$). Scale bars in A-C = 5 µm, BBox = bounding box.

Figure 5: Visualisation of primary cilia and cell cycle status in *R26Arl13b-Fucci2aR$^{+/Tg}$; CAG-Cre$^{+/Tg}$* embryos. Ubiquitous expression of the Arl13bCerulean-Fucci2a transgene was achieved by crossing *R26Arl13b-Fucci2aR* mice with ubiquitous *CAG-Cre* mice followed by whole mount confocal imaging of E7.5 and E8.5 embryos. **(A)** A representative Z-projection of a neural plate stage E7.5 *R26Arl13b-Fucci2aR$^{+/Tg}$; CAG-Cre$^{+/Tg}$* embryo. Cells of the proximal extraembryonic ectoderm are predominantly labelled with mCherry-hCdt1(30/120) and are starkly less proliferative compared to the distal embryonic visceral endoderm and epiblast lineages that contain a large proportion of cells in S/G2/M phases of the cell cycle labelled with mVenus-hGem(1/110). In all cases (n = 4, *R26Arl13b-Fucci2a^{Tg+}* E7.5 embryos from 3 litters) the node can be identified as a cluster of mCherry-hCdt1(30/120) positive cells at the distal pole of the embryo (boxed area). **(B)** A single plane of boxed area in A showing the node as a minor population of cells in G1/G0. Cells of the node are orientated perpendicular to the embryonic surface with mCerulean-ARL13B positive cilia pointing into a concave depression at the distal tip of the embryo (also see Figure S2). **(C)** A representative Z-projection of a 5S stage E8.5 *R26Arl13b-Fucci2a$^{+/Tg}$; CAG-Cre$^{+/Tg}$* prosencephalon (n = 8 *R26Arl13b-Fucci2a$^{+/Tg}$* E8.5 embryos from 2 litters)**.** The majority of cells on the surface and within the future forebrain are mVenus-hGem(1/110) positive many of which are ciliated. **(D)** A single plane of the boxed area in C showing a lateral ventricle. A high density of cilia are located in the lumen of the ventricle surrounded by mostly mVenus-hGem(1/110) positive neuroepithelial cells orientated perpendicular to the lumen (also see Figure S3). **(E)** A representative Z-projection of the rhombencephalic region of an E8.5 *R26Arl13b-Fucci2aR$^{+/Tg}$; CAG-Cre$^{+/Tg}$* embryo (n = 8

R26Arl13b-Fucci2a^{Tg+} E8.5 embryos from 2 litters). Emerging somites are clearly distinguishable as clusters of cycling cells labelled with mVenus-hGem(1/110) and mCherry-hCdt1(30/120). A high density of cilia are seen within each somite associated with cells in both G1 and S/G2/M phases of the cell cycle. Primary cilia are also identifiable on cycling cells outside of each somite. **(F)** Increased magnification of a single somite from boxed region in E (also see Figure S4). Scale bars in A, C, E = 100 μm, B and D = 50 μm and F = 25 μm.

Figure 6: Primary ependymal cultures exit the cell cycle and form multiple motile cilia during differentiation. Primary ependymal cultures were prepared from the ventricular zone of E18.5 *R26Arl13b-Fucci2aR*$^{+/Tg}$*; CAG-Cre*$^{+ve}$ embryos. Primary cell cultures were grown to confluency before being serum starved (Day 0) to induce differentiation. **(A-C)** Live imaging of cultures before serum starvation shows a mixture of cells in G1 and S/G2/M phases of the cell cycle labelled with mCherry-hCdt1(30/120) and mVenus-hGem(1/110) respectively. Primary cilia are present on a sub set of cells in all stages of the cell cycle. **(D-F)** Upon reaching confluency and following 7 days of serum starvation, all cells had dropped out of the cell cycle and were mCherry-hCdt1(30/120) positive. **(G-I)** Within the culture a subpopulation of cells had formed multiple motile cilia labelled with ARL13B-Cerulean (also see Movie S8). Scale bars in C, F and E = 50 μm, scale bar in I = 10 μm.

Figure 7: Primary cilia line the luminal surface of the airway epithelium during lung development. To confirm the ability to induce tissue specific expression of Arl13bCerulean-Fucci2a, *R26Arl13b-Fucci2aR* mice were crossed with endoderm specific Cre-recombinase expressing line *Sox17-2A-iCre.* Embryonic lungs were dissected from E11.5 embryos and imaged in *ex vivo* organotypic culture (n = 9 *R26Arl13b-Fucci2a*$^{Tg+}$ E11.5 embryos from 2 litters). **(A-C)** Arl13bCerulean-Fucci2a expression was restricted to the lung epithelium and a subset of migratory mesenchymal cells. In the proximal non-branching regions of the epithelium, cells are predominantly in G1 and ARL13B-Cerulean labelled cilia were visible along the entire length of the airway epithelium. **(D-F)** Magnification of the lung epithelium shows these cilia to be oriented into the lumen of branching tubules. **(G-I)** Regions of high proliferation can be identified at the

distal tips of the actively branching epithelium as shown by the high proportion of mVenus-hGem (1/110) labelled cells. Here also ARL13B-Cerulean labelled cilia are present in the lumen. Scale bars in B, C = 50 μm, scale bar in F = 10 μm.

STAR Methods:

Contact for Reagent and Resource Sharing

Further information and requests for resources and reagents should be directed to and will be fulfilled by the lead contact, Dr. Richard Mort (r.mort@lancaster.ac.uk).

Experimental Model and Subject Details

Mouse strains

All animal work was approved by a University of Edinburgh internal ethics committee and was performed in accordance with institutional guidelines under license by the UK Home Office (PPL 60/4424 and PPL 60/3785). Mice were maintained in the animal facilities of the University of Edinburgh. The *Sox17-2A-iCre* mouse line has been previously described (Engert *et al.*, 2009). Ubiquitous *CAG-Cre* mice used for germline activation of transgenes were generated by Dr D. A. Kleinjan (The University of Edinburgh) and were previously used in Mort et al (2014). *R26Arl13b-Fucci2aR* (MGI:6193732) and *R26Arl13b-Fucci2a* (MGI:6193734) mice were maintained on a C57BL/6J background, sex-matched and age-matched C57BL/6J stock animals were used as controls in adult analyses for changes in cilia length. Mice were genotyped using PCR as detailed below, they were housed in a barrier facility with 12 hour light and dark cycles.

Cell lines

Mouse Flp-In NIH 3T3 cells (male - Life Technologies) were cultured in Dulbecco's modified Eagle's medium (DMEM) containing; 10% fetal calf serum (FCS), 1% Penicillin/Streptomycin, 25 mM D-Glucose, 4 mM L-glutamine, 1 mM sodium pyruvate and 100 µg/ml Zeocin (Gibco). Mouse E14Tg2A embryonic stem cells (from mouse strain 129/Ola) were cultured in Glasgow's modified Eagle's medium (GMEM BHK-21) containing 10% FBS, 1% Sodium Pyruvate, 1% MEM non-essential amino acids, 2mM Glutamine, 0.1mM 2-Mercaptoethanol and 106 U/L LIF (prepared in house). Mouse embryonic fibroblasts were isolated from E12.5 embryos and maintained in Opti-mem (GIBCO), 10% v/v FCS, 1% v/v Penicillin/Streptomycin, 0.1mM 2-Mercaptoethanol (Sigma).

All cell lines were maintained in a humidified incubator at 37^0C supplied with 5% CO_2 in air.

Method Details

Construct design

The Fucci2 cell cycle probe pair consists of a fusion of mCherry with a truncated human CDT1 containing amino acids 30-120 and a fusion of mVenus and the 110 amino acid N-terminus of the human Geminin protein (Abe *et al.*, 2013). The bicistronic Fucci2a construct consists of the Fucci2 probes fused with a *Thosea asigna* virus 2A peptide (T2A) so that mCherry-hCdt1(30/120) is 5' of the T2A sequence and mVenus-hGem(1/110) is 3', therefore ensuring proper nuclear localisation of both probes (Mort *et al.*, 2014).

The *Arl13b* gene was amplified from mouse cDNA using the primers Arl13b_For and Arl1b_Rev (Table S1) and cloned into pmKate-N2 (Evrogen) as a HindIII/BamHI fragment. Arl13b was then transferred into the plasmid pCAG-H2BCerulean-Fucci2a (R. Mort, Unpublished) as an NheI/AgeI fragment replacing H2B with Arl13b. Subsequently pCAG-Arl13bCerulean-Fucci2a was cut with SalI, blunted and cut with KpnI; pCDNA5/Frt (Life Technologies) was cut with MluI, blunted and cut with KpnI allowing the transfer of CAG-Arl13bCerulean-p2a-Fucci2a as a Blunt/KpnI fragment into pCDNA5/Frt to yield the plasmid pCDNA5-CAG-Arl13bCerulean-Fucci2a. To generate pRosa26-CAG-floxNeo-Arl13bCerulean-Fucci2a, Arl13bCerulean-p2a was PCR amplified using the primers Arl13bCerulean_For and Arl13bCerulean_Rev and cloned as an MluI/BssHII fragment into the single MluI site of the previously described pRosa26-CAG-floxNeo-Fucci2a plasmid (Mort *et al.*, 2014). The transgene was orientated in opposition to the endogenous *Rosa26* promoter to avoid transcriptional interference (Strathdee, Ibbotson and Grant, 2006).

Generation of Arl13bCerulean-Fucci2a NIH 3T3 cells

The Arl13bCerulean-Fucci2a 3T3 cell line was generated using the Flp-In system (Life

Technologies). The Neon electroporation system (Life Technologies) was used to co-transfect the cells with pCDNA5-CAG-Arl13bFucci2a and the pOG44 Flp recombinase expressing plasmid (Life Technologies). Cells were trypsinised, washed in PBS and resuspended in Buffer R. 18 µg of pOG44 and 2 µg of pCDNA5-CAG-Arl13bCerulean-Fucci2a were added to each tube. Each tube was then split into 2 × 100 ul electroporations (2 pulses: 1,350 V, 20 ms) and pooled into a single T75 flask containing pre-warmed OPTIMEM (Life Technologies) and incubated overnight. On the second day cells were transferred into DMEM containing, 10% v/v fetal calf serum (FCS), 1% v/v Penicillin/Streptomycin and 100 µg/ml Hygromycin B. After 14 days of Hygromycin B selection the polyclonal cell line was passaged and used for subsequent analyses.

Cell cycle analysis by FACS

Confirmation of correct cell cycle phase representation by Fucci2 fluorescence was performed by FACS using DAPI intensity as a measure of DNA content. Using a FACS Aria2 SORP cell sorter (Becton Dickinson) cells were sorted into mVenus (488nm laser, 525/50nm bandpass filter) and mCherry (560nm laser, 610/20nm band pass filter) positive populations. Cells were fixed in 70% ethanol overnight at -20ºC. The next day cells were stained with DAPI (5 µg/ml in PBS) and DNA content analysed using the 405 nm laser and 450-50 nm bandpass filter. FACSDiVa Version 6.1 (BD) was used to analyse the data.

Arl13bCerulean-Fucci2a NIH 3T3 cell migration assay

In order to determine the orientation of primary cilia during migration, Ar13bCerulean-Fucci2a NIH 3T3 cells were seeded at high density into a custom-made silicon ring mounted on a 24-well glass bottomed plate (Greiner Bio-one) by surface tension. The next day the silicon ring was removed and the media replaced with phenol free DMEM (Millipore) (10% v/v FCS, 1% v/v Penicillin/Streptomycin). Images were taken every 10 mins at a single Z plane. The angle of cilia in relation to the centre of the nucleus was measured in migrating cells after 5 and 10 hours using a custom macro in ImageJ. The angle was then corrected for the orientation of the wound edge with respect to the image. A control experiment was also set up in parallel in which

Arl13bCerulean-Fucci2a NIH 3T3 cells were seeded so there was no directional movement and their ciliary angles measured.

Mouse embryonic stem cell targeting

E14Tg2a ES cells were electroporated with linearised pRosa26-CAG-floxNeo-Arl13bCerulean-Fucci2a plasmid using standard procedures. Clones were picked after 14 days of G418 selection. Long range PCR across the 5' and 3' homology arms confirmed correct targeting of the endogenous *Rosa26* locus without further genomic rearrangements. Screening across the Rosa26 5′ homology arm (35 cycles: denaturation - 98 ℃ for 10 secs; annealing - 66 ℃ for 10 secs; extension - 72 ℃ for 30 secs) was performed using the primers Xu_Wt_For (Hohenstein *et al.*, 2008) and Rosa5_R1 (Mort *et al.*, 2014) (Figure S1A) to generate a 1.4 kb targeted band. A second control PCR (35 cycles: denaturation - 98 ℃ for 10 secs; annealing - 60 ℃ for 10 secs; extension - 72 ℃ for 30 secs) was conducted to demonstrate DNA integrity using the primers Wt_For and Wt_Rev (Soriano, 1999) to generate a 450 bp wild type band from the Rosa26 locus. Correct targeting was confirmed on the positive clones by PCR amplification (35 cycles: denaturation - 98 ℃ for 10 secs; annealing - 68 ℃ for 10 secs; extension - 72 ℃ for 30 secs) of a 4 kb targeted band across the Rosa26 3′ homology arm using the primers Rosa3_F1 and Rosa3_R2, all primer sequences are outlined in Table S1. All PCR reactions were carried out using 50 ng genomic DNA using Phusion Hotstart II DNA polymerase (Thermo Fisher Scientific) with GC buffer according to the manufacturers standard reaction conditions.

Cre-activation of *R26Arl13b-Fucci2aR* mouse embryonic stem cell lines

Correct expression of the Arl13bCerulean-Fucci2a transgene was assessed in targeted mESC clones by transfection with the PGK-Cre plasmid followed by selection of fluorescent clones and confirmation of G418 sensitivity. To excise the neomycin stop cassette and activate Arl13bCerulean-Fucci2a expression, 1 x 10^7 *R26Arl13b-Fucci2aR* mESCs in 0.5 ml of PBS were combined with 100 µg PGK-Cre plasmid (a kind gift from Dr Laura Lettice, University of Edinburgh) and incubated on ice for 15 minutes. Cells were transferred to an ice-cold 0.4 mm

electroporation cuvette and electroporated using the Gene Pulser II (Bio-Rad). Cells were seeded at low density (1000 cells per 10 cm^2 pre-gelatinised plate), and grown until clones become visible. Fluorescent clones were picked, expanded and checked for G418 sensitivity (250 µg/ml).

2i conversion of *R26Arl13b-Fucci2a* mouse embryonic stem cells

2i conversion was achieved by culturing for a minimum of 7 days in 50/50 neurobasal (Gibco) / DMEM/F12 (Gibco) media containing 1 X N2 Supplement (Gibco), 1 X B27 + RA (Gibco), 7.5% w/v BSA (Gibco), 1 X Penicillin/Streptomycin (Corning), 1 µM PD0325901 (Stemgent), 3 µM CHIR99021 (Stemgent), 2mM Glutamine (Gibco), 0.15 mM Monothioglycerol (Sigma) and 1000 U/ml LIF (Esgro). 2i culture conditions are as reported in Ying et al. (2008) with the exception of ESGRO LIF (Millipore) used at 1000 U/ml.

Generation of *R26Arl13b-Fucci2aR* mice

Transgenic mice were produced by blastocyst injection of *R26Arl13b-Fucci2aR* ES cells according to standard methods using C57BL/6J mice. Germline transmission was identified after a single round of ES cell blastocyst injections. Subsequent intercrosses generated *R26Arl13b-Fucci2aR*$^{+/+}$, *R26Arl13b-Fucci2aR*$^{+/Tg}$ and *R26Arl13b-Fucci2aR*$^{Tg/Tg}$ offspring at Mendelian ratios. *R26Arl13b-Fucci2aR* mice were genotyped using the strategy described for *R26Fucci2aR* animals (Mort *et al.*, 2014). Briefly, a duplex PCR reaction (35 cycles: denaturation - 98℃ for 10 secs; annealing - 68℃ for 10 secs; extension - 72℃ for 30 secs) was used with primers R26_Wt_For, R26_Wt_Rev and F2A_Rev (Table S1), reactions were carried out using Phusion Hotstart II DNA polymerase (Thermo Fisher Scientific) with GC buffer according to the manufacturers standard reaction conditions the R26_Wt_Rev primer was used at 50 µM rather than 100 µM. The *R26Arl13b-Fucci2aR* allele was bred to homozygosity and loss of the wild type allele confirmed by PCR to further validate our ES cell screening strategy.

Preparation of primary ependymal cultures

To isolate primary ependymal cells, the ventricular zone from E18.5 *R26Arl13b-Fucci2aR*$^{+/Tg}$*; CAG-Cre*$^{+/Tg}$ embryos was dissected and dissociated by mild trypsinisation in a solution of trypsin/EDTA for 45 minutes followed by pipetting to form a single cell solution. Cells were then seeded onto a collagen-coated glass bottom dish. Cells were cultured in DMEM (10 % v/v FCS, 1 % v/v Pen/Strep, 1 X GlutMax) until confluent and then serum starved to induce differentiation and the formation of multiple motile cilia.

Preparation of mouse embryonic fibroblasts

Mouse embryonic fibroblasts (MEFs) were prepared from individual E12.5 embryos using standard techniques. Briefly, the tail, limbs, head and organs were removed and the remainder of the body transferred to a 6-well plate on ice. In a cell culture hood using sterile techniques the PBS was aspirated off and replaced with 50/50 trypsin/versene. The embryos were then broken up into small pieces using forceps and left for 1 hour, 3 ml of MEF media (Opti-mem (GIBCO), 10 % v/v FCS, 1 % v/v Penicillin/Streptomycin, 0.1 mM 2-Mercaptoethanol (Sigma)) was added and solution pipetted up and down to dissociate the tissue into single cells and seeded into a T75 tissue culture flask. MEF lines were passaged at least 3 times before being stored in liquid nitrogen in MEF media plus 10 % v/v DMSO, 30% v/v FCS. MEF lines were cultured in a humidified 37 ^{o}C incubator supplied with 5 % CO2, maintained at high confluency and split at no greater ratio than 1:3.

Bile duct isolation and enrichment:

Livers were flushed with phosphate buffered saline through perfusion through the inferior vena cava, then dissected, and digested in DMEM/F12 media containing Collagenase IV (Gibco) and Dispase (Gibco) at 37 ^{o}C with intermittent agitation until the parenchyma was digested away and the bile ducts appeared visible in the media. Following digestion, bile ducts were collected using a 70 µm filter. Serial PBS washing removed residual cells and resulting bile ducts were used for both live and fixed imaging. For live imaging, bile ducts were suspended in DMEM^{gfp}-2 anti-bleaching live cell visualization medium supplemented with rutin (20 mg/L - Evrogen), and

NucBlue (Invitrogen) and incubated for 30 minutes at 37 °C. Live imaging was performed on an Andor Dragonfly Dual Spinning Disc confocal microscope. For quantitative imaging of cilia length, isolated bile ducts were fixed for 10 minutes in methacarn and permeabilised with PBS + 0.1 % Tween20 prior to incubating in protein block for 1 hour. Primary antibodies were allowed to incubate overnight at 4 °C and secondary antibodies for two hours at room temperature following PBS washes. Bile ducts were fixed and imaged using confocal microscopy (Nikon A1R+). For organoids, isolated bile ducts were plated with 100 % GFR Matrigel (Corning) and cultured in base media (DMEM/F12 with Glutamax, Antibiotic-Antimycotic and HEPES (Gibco)) or growth media (base media supplemented with EGF, HGF, FGF10 (Peprotech), Gastrin, Nicotinamide, N-Acetylcystine, A83-01 (TGFβ inhibitor; Sigma), B-27 (Gibco), Forskolin, Y-27632 (Rock inhibitor; Tocris), and Chir99021 (GSK3β inhibitor; Miltenyl)).

Fluorescence microscopy and live imaging

Fluorescence live cell imaging of cell lines and embryonic tissue was performed on the stage of a Nikon A1R confocal microscope surrounded by an environmental chamber providing 5 % CO_2 in air and maintained at a constant stage top temperature of 37 °C. Data was acquired using either a 20x Plan Apochromat VC 0.5 DIC N2, 40x Plan Fluar 0.75 DIC N2 or 60x Plan Apochromat VC 1.2 WI DIC N2 lens through NIS Elements AR software (Nikon Instruments Europe, Netherlands). The scission studies and cilia length comparisons were performed using the multimodal Imaging Platform Dragonfly (Andor Technologies, Belfast UK) using 20x Plan Apochromat VC 0.75 DIC N2 or air 40x Plan Fluar 0.75 DIC N2. Data were collected in Spinning Disk 25 µm pinhole mode on the high sensitivity iXon888 EMCCD camera. Z stacks were collected using a Mad City Labs Piezo. Data was visualized using IMARIS 8.4 (Bitplane). In our time-lapse dataset, we identified cilia using segmentation and morphological filtering and defined each cilia by a bounding box (the minimum bounding rectangular cuboid that fully encompasses the cilia). The following laser lines and band filters were used; Cerulean – 458 nm, 482/35 (A1R) or 480/40 (Dragonfly); mVenus – 514 nm, 540/30 (A1R) or 620/60 (Dragonfly); mCherry – 561 nm, 595/50 (A1R) or 700/75 (Dragonfly). Cells and tissue were imaged in phenol free DMEM

(Millipore) (10% v/v FCS, 1% v/v Penicillin/Streptomycin, 1 X GlutMax) on glass bottomed plates (Greiner Bio-one) except imaging of whole-mount embryos which were imaged in DMEM (50 % v/v rat serum, 1 % v/vPenicillin/Streptomycin, 1 X GlutaMax) and embryonic lung cultures which were embedded in 50 % matrigel:media and mounted on a Lumox membrane (Greiner Bio-one) in a custom built imaging chamber (Mort, Hay and Jackson, 2010).

Immunofluorescence and comparison of cilia length

To compare cilia length between *R26Arl13b-Fucci2a*$^{Tg+}$ and control mice, tissues were dissected and half maintained in cold PBS for live imaging (see above) while the other half was fixed in 4 % w/v PFA/PBS for one hour and cryoprotected though a sucrose/PBS gradient overnight at 4 ^{o}C before embedding in OCT (Sciegen). Nasal brushings were taken by exposing the nasal septum and scraping cells off the epithelium with an interdental brush (TePe, 0.8 mm ExtraSoft) followed by resuspension in DMEM (isolated from animals at P7-P60). Cells were spread on Superfrost slides, and imaged directly or processed for immunofluorescence. Fixed tissues were embedded in OCT (Scigen, USA) and used for cryo-sectioning. Sections of 12 μm were mounted on Superfrost glass slides, air dried and stored at -80 or used immediately. For immunofluorescence, slides were submerged in PBS to remove excess of mounting media and briefly fixed for 2 mins in 4 % w/v PFA/PBS, washed and permeabilised with 0.25% v/v Triton/PBS for 10 minutes. Slides were then washed and blocked in 2-4 % w/v BSA, 0.05 % v/v Tween-20 in PBS. Primary and secondary antibodies were incubated in the same solution for one hour at room temperature before washing and mounting in Prolong Gold (Invitrogen) for imaging.

Image analysis

Image analysis tasks were performed either on Imaris (Bitplane) or using custom written macros for the Fiji distribution of ImageJ, an open source image analysis package based on NIH Image (Schneider et al., 2012).

Quantification and Statistical Analysis

Statistical tests were performed using the ‘R’ statistics package, an open source software package based on the ‘S’ programming language (http://www.R-project.org) or with GraphPad Prism. The n value and definition of n along with the statistical test used is indicated in the figure legend of each figure.

Supplemental Information titles and legends:

Movie S1, related to Figure 1. Left panel: Stable Arl13bCerulean-Fucci2a NIH 3T3 cells progressing through the cell and cilia cycles. **Right panel:** A single Arl13bCerulean-Fucci2a NIH 3T3 cell (arrow in frame 1) progresses through the cell cycle and divides to form two ciliated daughter cells (arrows in final frame). The cilia in the mother persists until late G2.

Movie S2, related to Figure 3. Ciliated migrating Arl13bCerulean-Fucci2a NIH 3T3 cells in a migration assay.

Movie S3, related to Figure 4. Scission of primary cilia in G1 Arl13bCerulean-Fucci2a NIH 3T3 cells after serum starvation.

Movie S4, related to Figure 4. Destabilisation of primary cilia after addition of the F-actin inhibitor CK-666 in serum starved Arl13bCerulean-Fucci2a NIH 3T3 cells.

Movie S5, related to Figure 4. Anterograde and retrograde movement of cilia bulges in Arl13bCerulean-Fucci2a NIH 3T3 cells treated with CK-666.

Movie S6, related to Figure 5. Optical confocal sectioning of an E8.5 *R26Arl13b-Fucci2aR*$^{Tg/+}$*; CAG-Cre*$^{Tg/+}$ mouse forebrain.

Movie S7, related to Figure 5. Motile cilia beating on differentiated primary mouse ependymal cultures derived from a *R26Arl13b-Fucci2aR*$^{Tg/+}$*; CAG-Cre*$^{Tg/+}$ mouse.

Movie S8. Adult bile duct organoids isolated from preps used for Figure S2K (N=3 animals, 4 months), were expanded and were cultured in 50 % growth/ 50 % basal media for 16 hours for imaging, one stack every 20 minutes. Many mVenus-hGem(1/110)+ cells are observed with ARL13B+ cilia. Zoomed in regions of interest show (1) a rapid loss of a cilia just prior to mitosis and (2) asymmetric rates of ciliation between daughters in organoids.

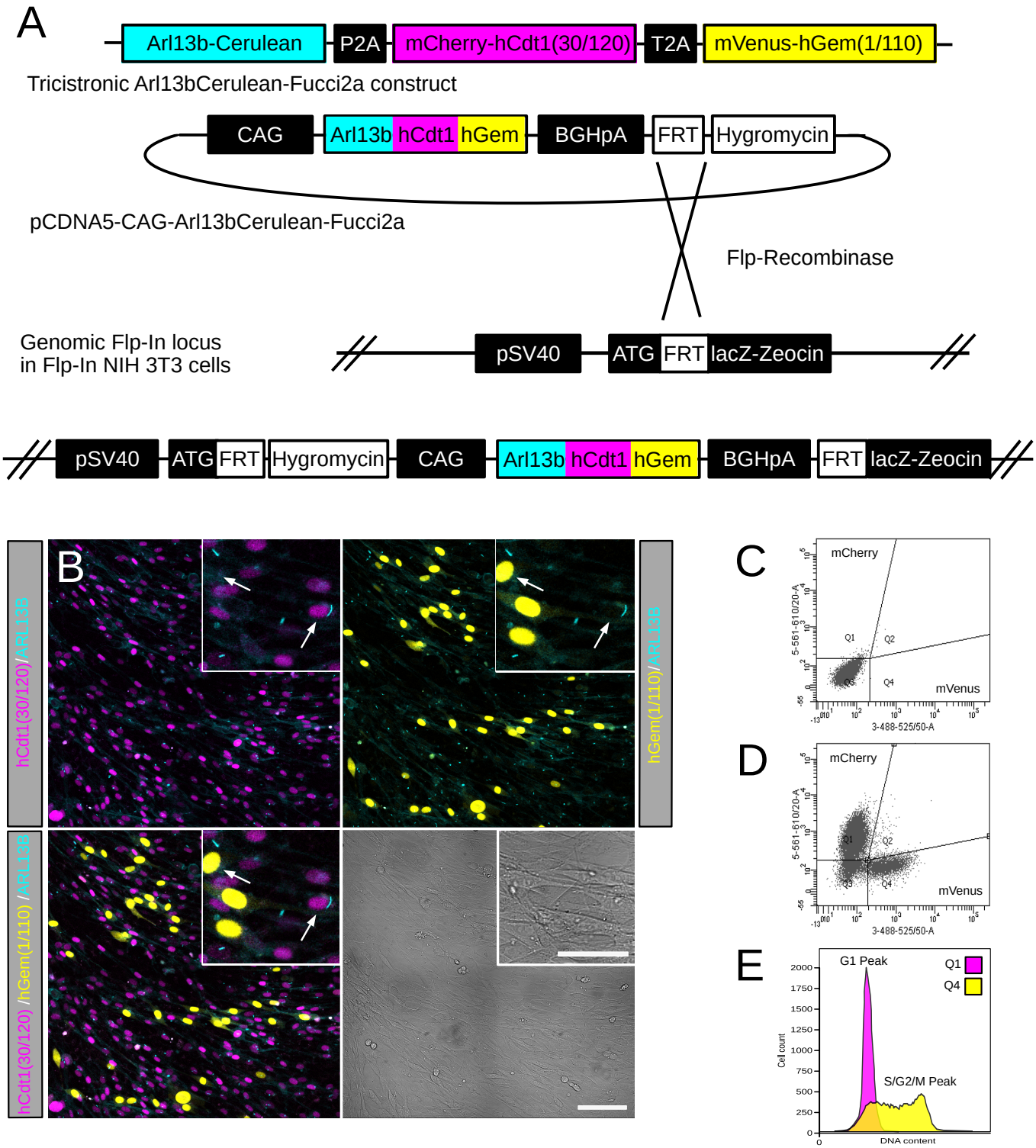
A
Arl13b-Cerulean
P2A
mCherry-hCdt1(30/120)
T2A
mVenus-hGem(1/110)
Tricistronic Arl13bCerulean-Fucci2a construct
CAG
Arl13b
hCdt1
hGem
BGHpA
FRT
Hygromycin
pCDNA5-CAG-Arl13bCerulean-Fucci2a
Flp-Recombinase
Genomic Flp-In locus
in Flp-In NIH 3T3 cells
pSV40
ATG
FRT
lacZ-Zeocin
pSV40
ATG
FRT
Hygromycin
CAG
Arl13b
hCdt1
hGem
BGHpA
FRT
lacZ-Zeocin
B
hCdt1(30/120)/ARL13B
hGem(1/110)/ARL13B
hCdt1(30/120) /hGem(1/110) /ARL13B
C
mCherry
mVenus
Q1
Q2
Q3
Q4
5-561-610/20-A
3-488-525/50-A
D
mCherry
mVenus
Q1
Q2
Q3
Q4
5-561-610/20-A
3-488-525/50-A
E
G1 Peak
S/G2/M Peak
Q1
Q4
Cell count
DNA content
2000
1750
1500
1250
1000
750
500
250
0

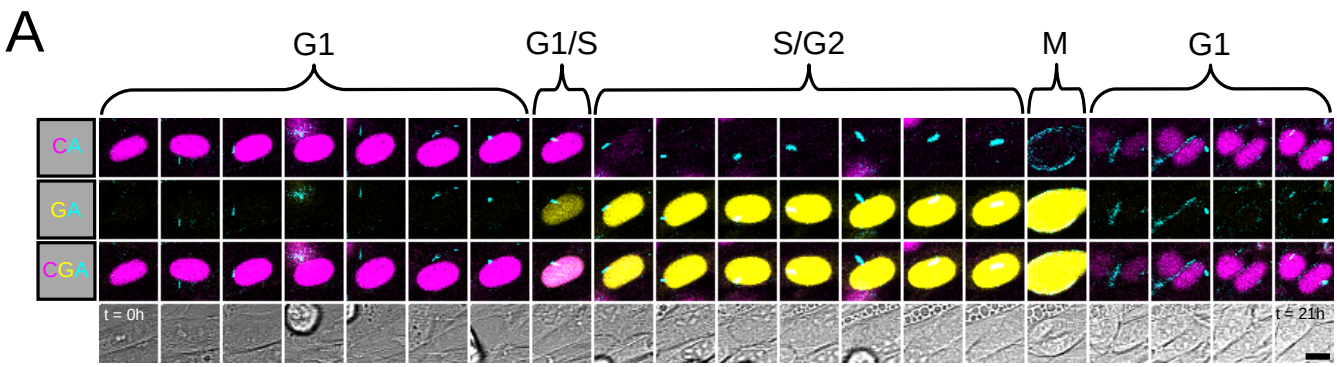
A
G1
G1/S
S/G2
M
G1
CA
GA
CGA
t = 0h
t = 21h

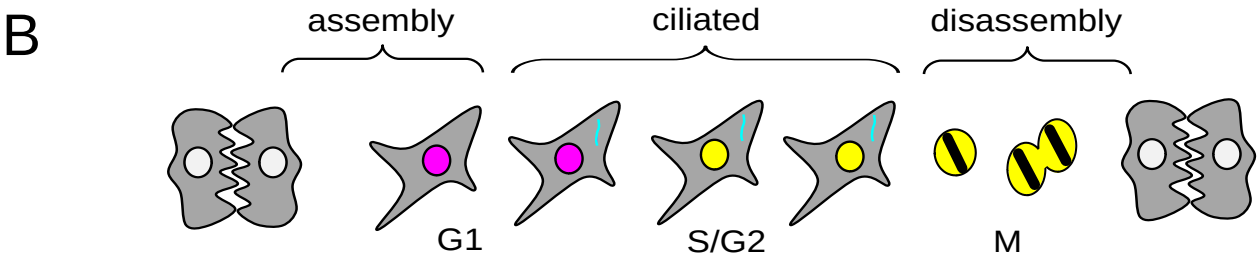
B
assembly
ciliated
disassembly
G1
S/G2
M

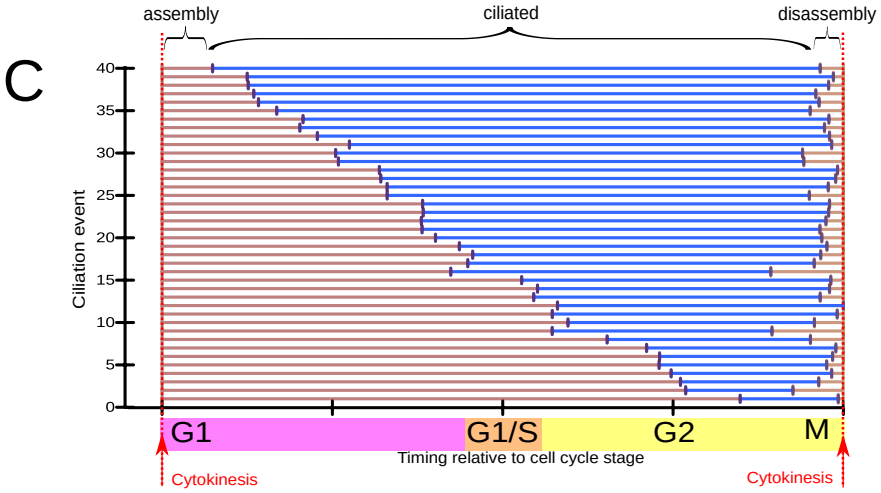
C
assembly
ciliated
disassembly
Ciliation event
G1
G1/S
G2
M
Timing relative to cell cycle stage
Cytokinesis
Cytokinesis

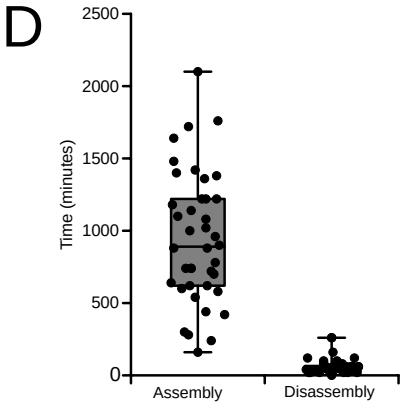
D
Time (minutes)
Assembly
Disassembly

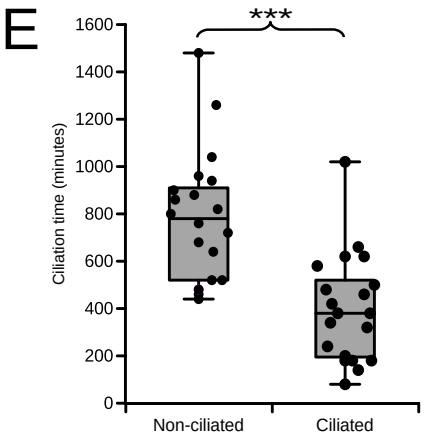
E
***
Ciliation time (minutes)
Non-ciliated
Ciliated

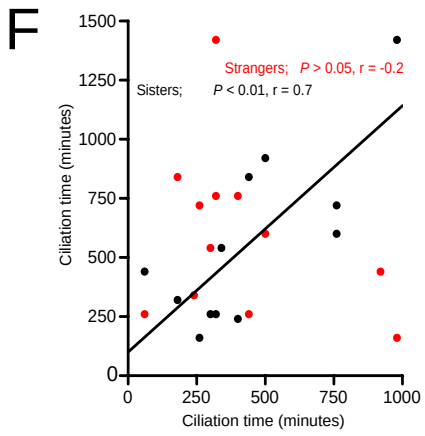
F
Strangers; P > 0.05, r = -0.2
Sisters; P < 0.01, r = 0.7
Ciliation time (minutes)
Ciliation time (minutes)

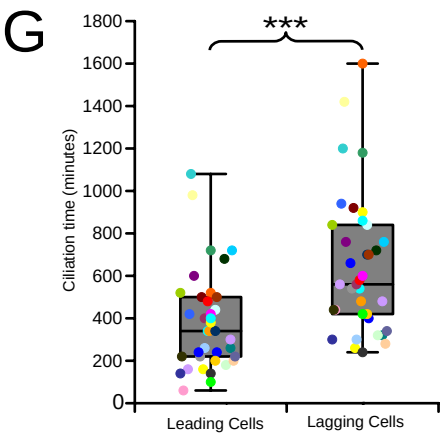
G
***
Ciliation time (minutes)
Leading Cells
Lagging Cells

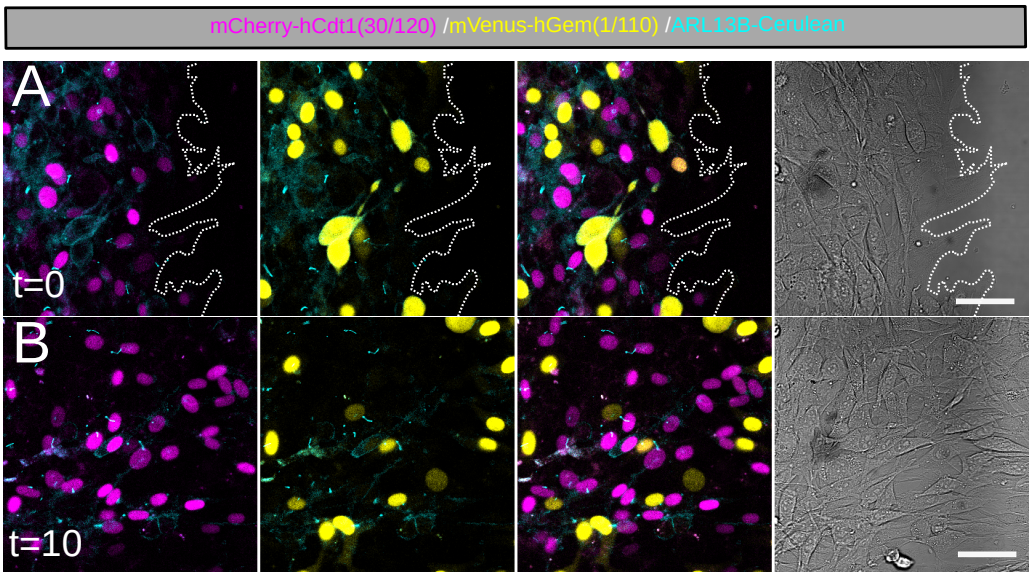
mCherry-hCdt1(30/120) /mVenus-hGem(1/110) /ARL13B-Cerulean
A
t=0
B
t=10

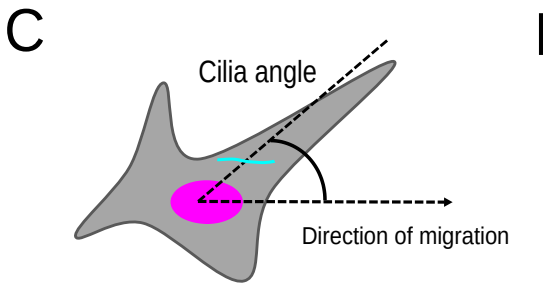
C
Cilia angle
Direction of migration

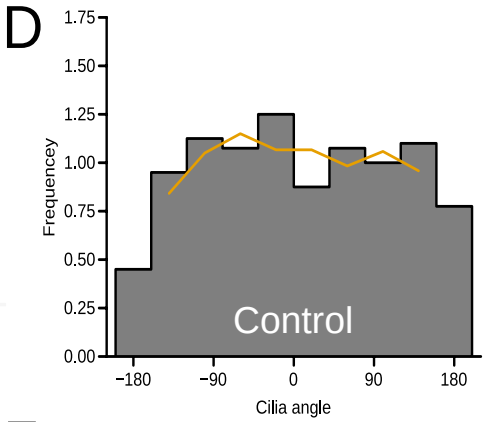
D
Frequencey
Control
Cilia angle

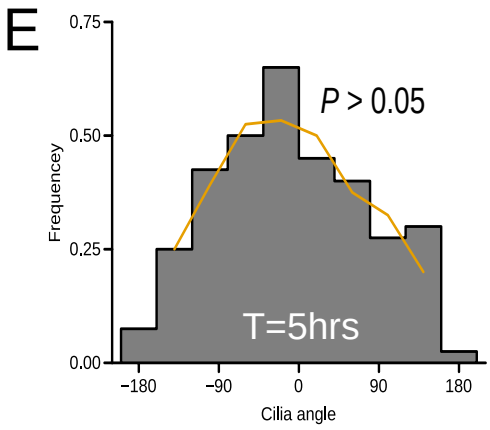
E
Frequencey
P > 0.05
T=5hrs
Cilia angle

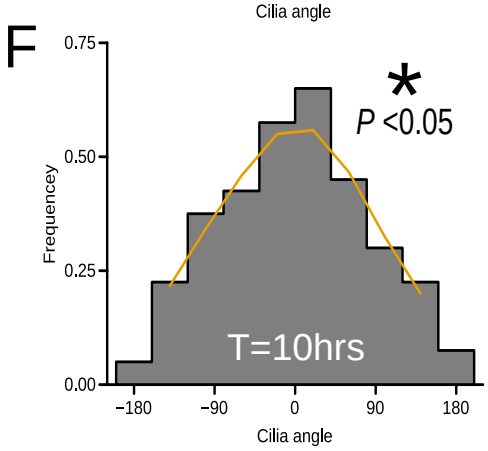
F
Frequencey
*
P <0.05
T=10hrs
Cilia angle

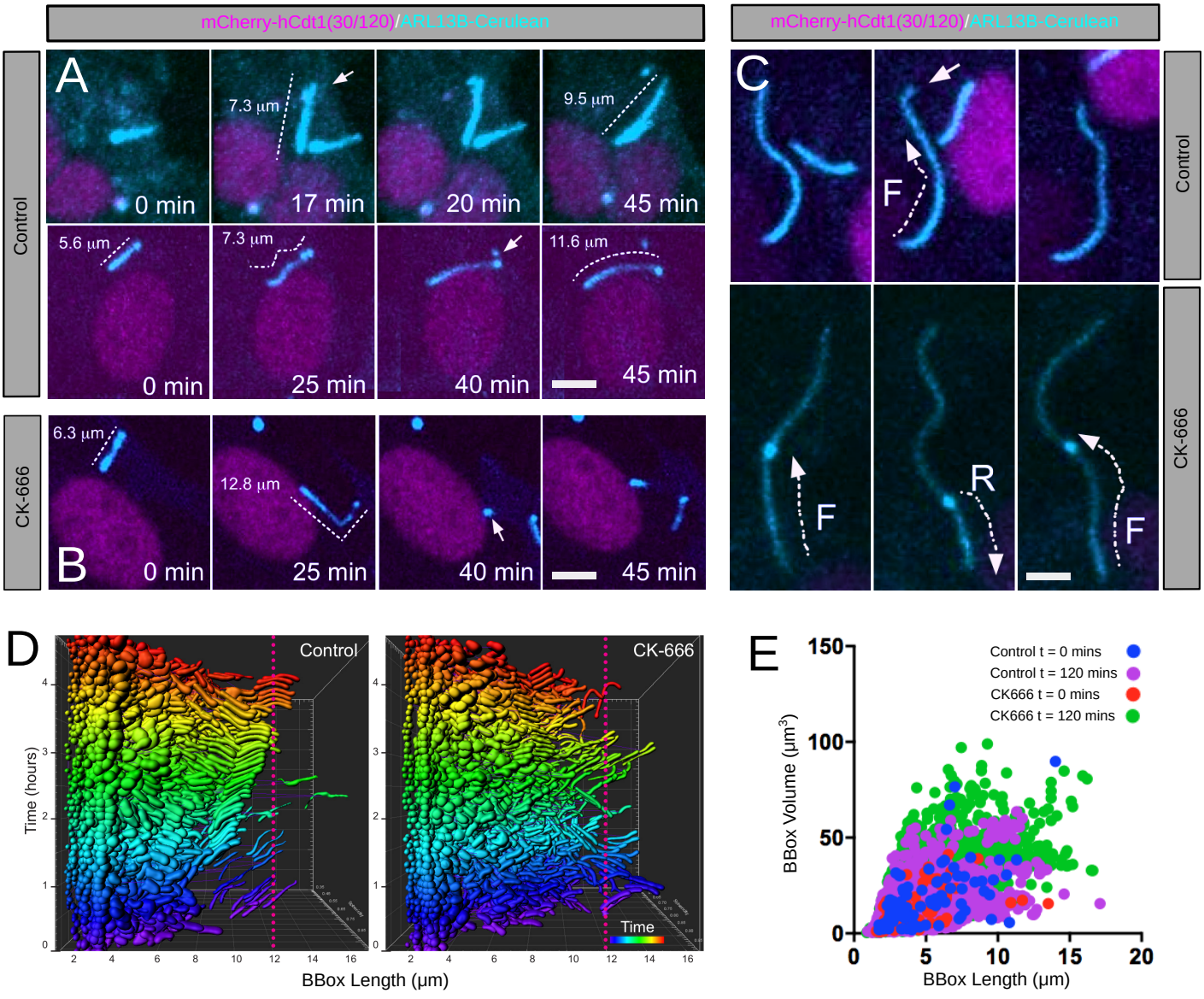
mCherry-hCdt1(30/120)/ARL13B-Cerulean
Control
A
0 min
7.3 μm
17 min
20 min
9.5 μm
45 min
5.6 μm
0 min
7.3 μm
25 min
40 min
11.6 μm
45 min
CK-666
B
6.3 μm
0 min
12.8 μm
25 min
40 min
45 min
mCherry-hCdt1(30/120)/ARL13B-Cerulean
C
F
Control
F
R
F
CK-666

D
Control
CK-666
Time (hours)
BBox Length (μm)
Time

E
Control t = 0 mins
Control t = 120 mins
CK666 t = 0 mins
CK666 t = 120 mins
BBox Volume (μm³)
BBox Length (μm)

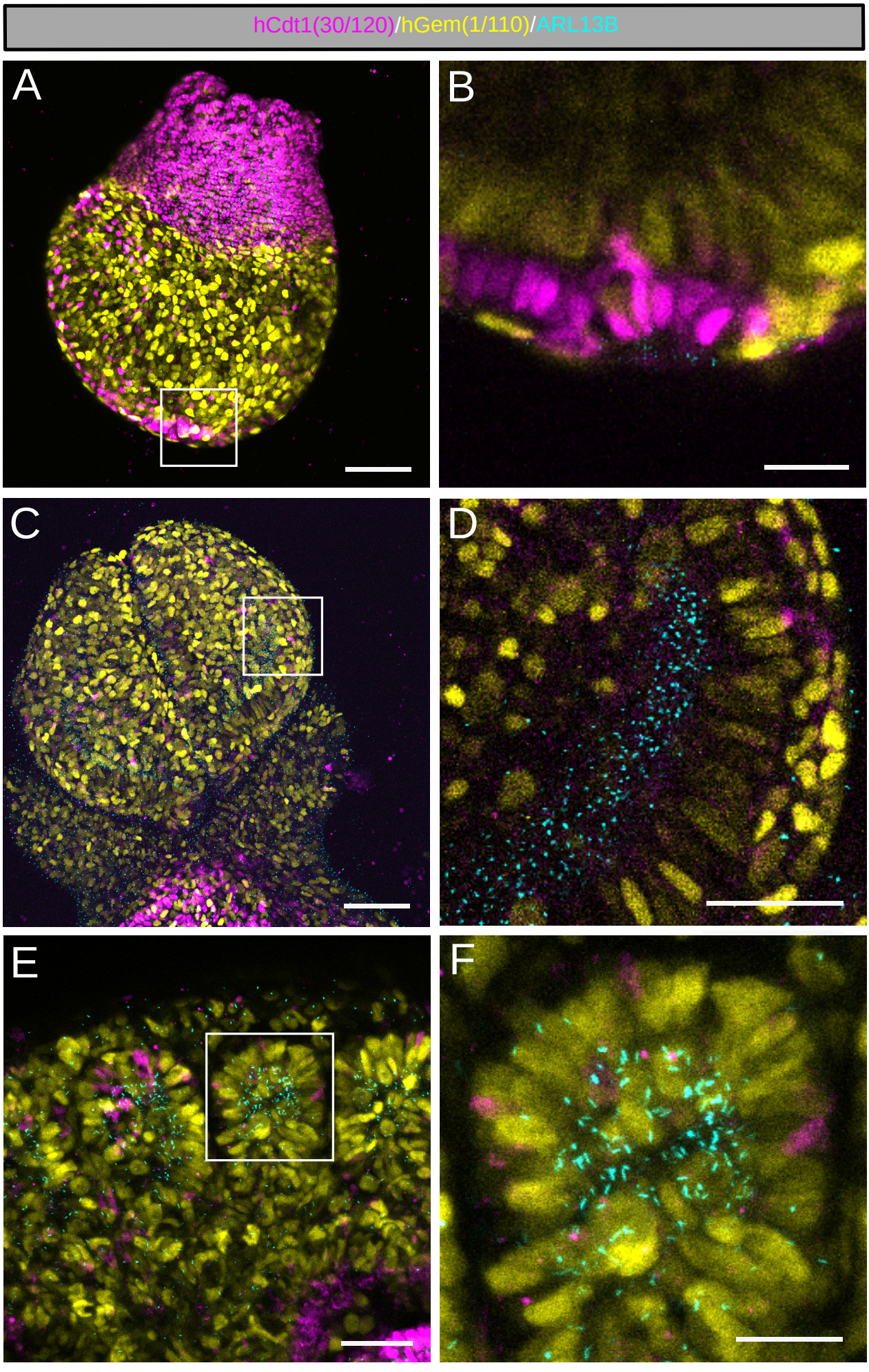
hCdt1(30/120)/hGem(1/110)/ARL13B
A
B
C
D
E
F

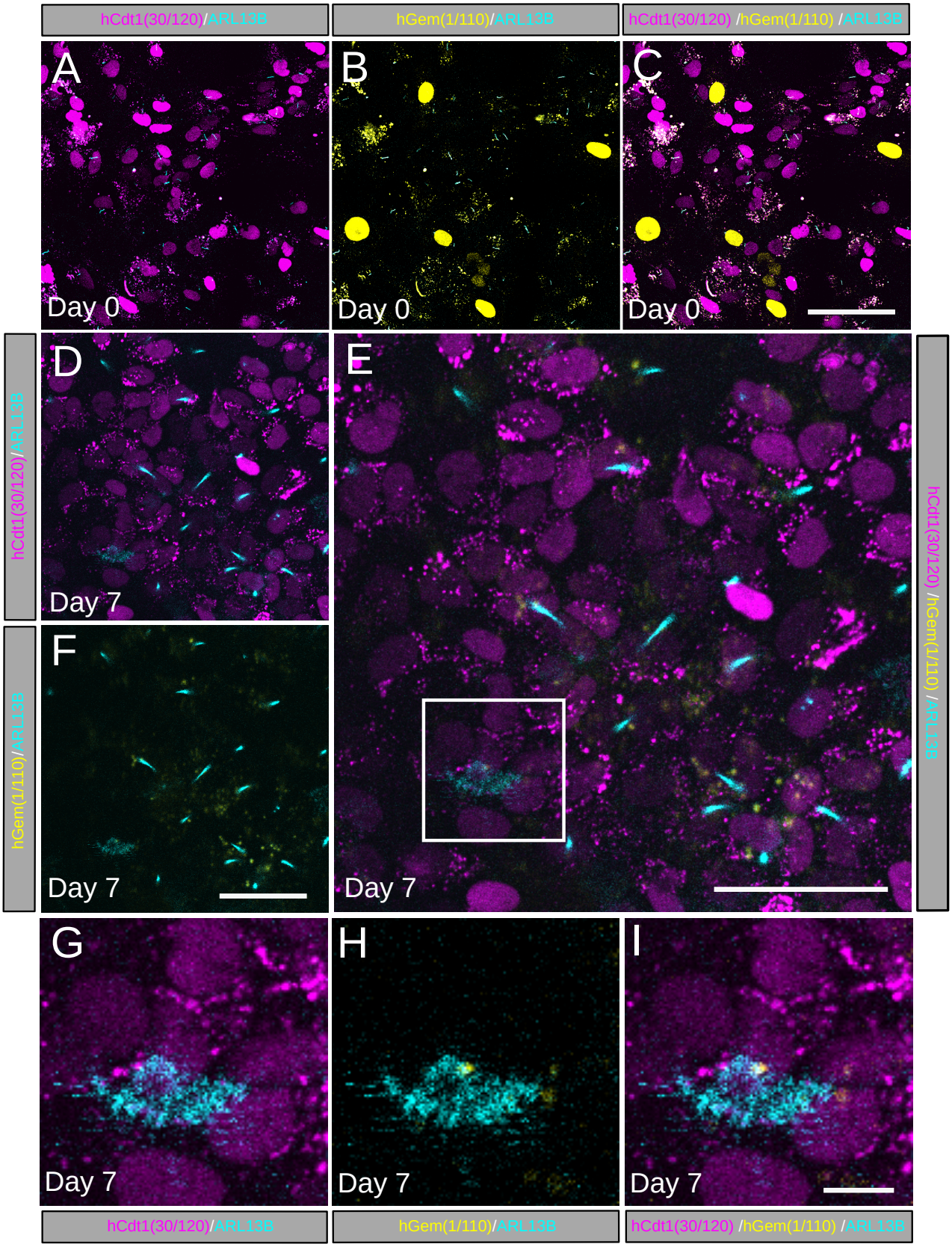
hCdt1(30/120)/ARL13B
hGem(1/110)/ARL13B
hCdt1(30/120) /hGem(1/110) /ARL13B
A
Day 0
B
Day 0
C
Day 0
hCdt1(30/120)/ARL13B
D
Day 7
E
Day 7
hCdt1(30/120) /hGem(1/110) /ARL13B
hGem(1/110)/ARL13B
F
Day 7
G
Day 7
H
Day 7
I
Day 7
hCdt1(30/120)/ARL13B
hGem(1/110)/ARL13B
hCdt1(30/120) /hGem(1/110) /ARL13B

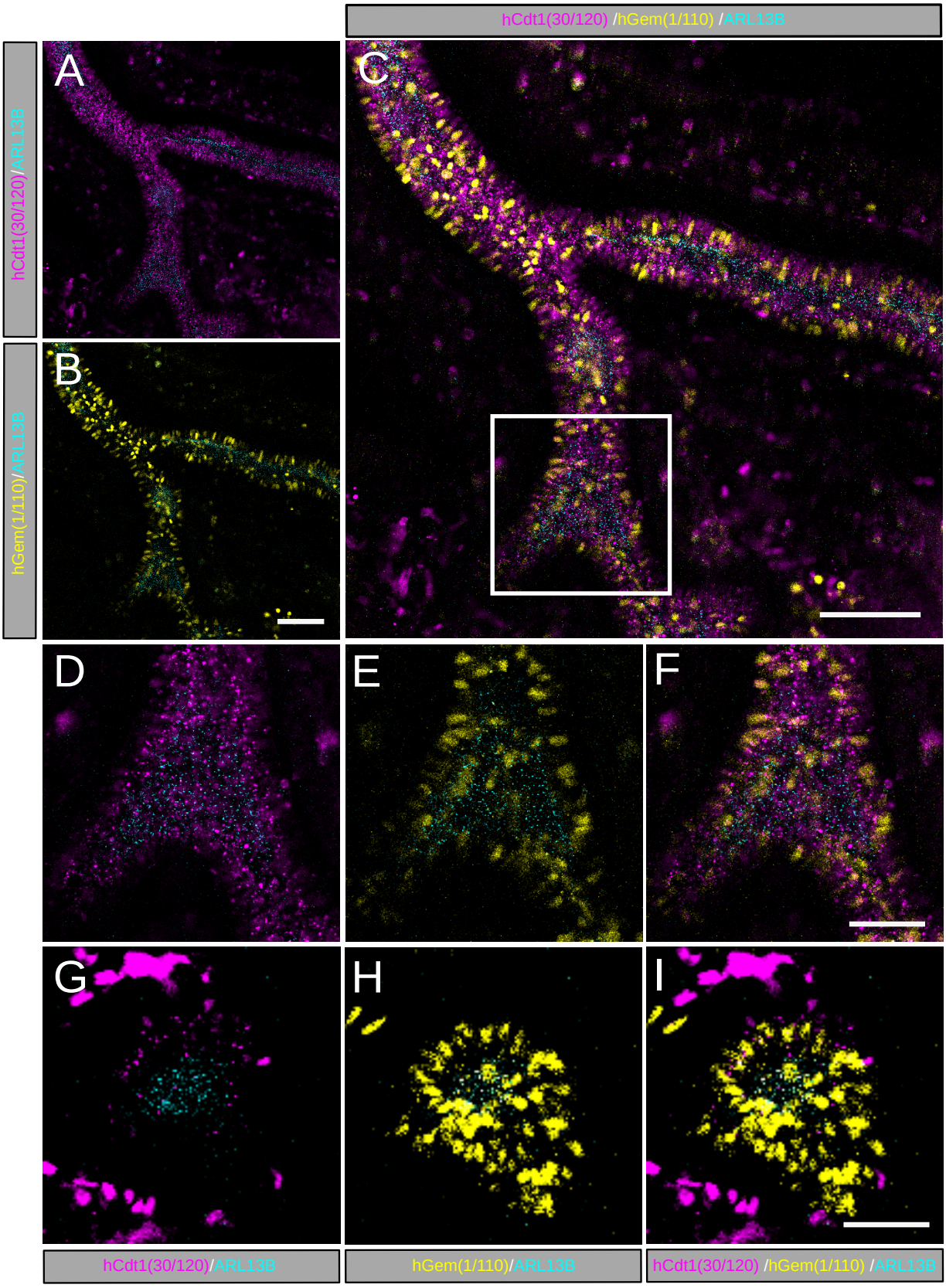
hCdt1(30/120) /hGem(1/110) /ARL13B
hCdt1(30/120)/ARL13B
hGem(1/110)/ARL13B
A
B
C
D
E
F
G
H
I
hCdt1(30/120)/ARL13B
hGem(1/110)/ARL13B
hCdt1(30/120) /hGem(1/110) /ARL13B

KEY RESOURCES TABLE

The table highlights the genetically modified organisms and strains, cell lines, reagents, software, and source data **essential** to reproduce results presented in the manuscript. Depending on the nature of the study, this may include standard laboratory materials (i.e., food chow for metabolism studies), but the Table is **not** meant to be comprehensive list of all materials and resources used (e.g., essential chemicals such as SDS, sucrose, or standard culture media don't need to be listed in the Table). **Items in the Table must also be reported in the Method Details section within the context of their use.** The number of **primers and RNA sequences** that may be listed in the Table is restricted to no more than ten each. If there are more than ten primers or RNA sequences to report, please provide this information as a supplementary document and reference this file (e.g., See Table S1 for XX) in the Key Resources Table.

Please note that ALL references cited in the Key Resources Table must be included in the References list. Please report the information as follows:

- **REAGENT or RESOURCE:** Provide full descriptive name of the item so that it can be identified and linked with its description in the manuscript (e.g., provide version number for software, host source for antibody, strain name). In the Experimental Models section, please include all models used in the paper and describe each line/strain as: model organism: name used for strain/line in paper: genotype. (i.e., Mouse: OXTR$^{fl/fl}$: B6.129(SJL)-Oxtr$^{tm1.1Wsy/J}$). In the Biological Samples section, please list all samples obtained from commercial sources or biological repositories. Please note that software mentioned in the Methods Details or Data and Software Availability section needs to be also included in the table. See the sample Table at the end of this document for examples of how to report reagents.

- **SOURCE:** Report the company, manufacturer, or individual that provided the item or where the item can obtained (e.g., stock center or repository). For materials distributed by Addgene, please cite the article describing the plasmid and include "Addgene" as part of the identifier. If an item is from another lab, please include the name of the principal investigator and a citation if it has been previously published. If the material is being reported for the first time in the current paper, please indicate as "this paper." For software, please provide the company name if it is commercially available or cite the paper in which it has been initially described.

- **IDENTIFIER:** Include catalog numbers (entered in the column as "Cat#" followed by the number, e.g., Cat#3879S). Where available, please include unique entities such as RRIDs, Model Organism Database numbers, accession numbers, and PDB or CAS IDs. For antibodies, if applicable and available, please also include the lot number or clone identity. For software or data resources, please include the URL where the resource can be downloaded. Please ensure accuracy of the identifiers, as they are essential for generation of hyperlinks to external sources when available. Please see the Elsevier list of Data Repositories with automated bidirectional linking for details. When listing more than one identifier for the same item, use semicolons to separate them (e.g. Cat#3879S; RRID: AB_2255011). If an identifier is not available, please enter "N/A" in the column.
    - ***A NOTE ABOUT RRIDs:*** We highly recommend using RRIDs as the identifier (in particular for antibodies and organisms, but also for software tools and databases). For more details on how to obtain or generate an RRID for existing or newly generated resources, please visit the RII or search for RRIDs.

Please use the empty table that follows to organize the information in the sections defined by the subheading, skipping sections not relevant to your study. Please do not add subheadings. To add a row, place the cursor at the end of the row above where you would like to add the row, just outside the right border of the table. Then press the ENTER key to add the row. Please delete empty rows. Each entry must be on a separate row; do not list multiple items in a single table cell. Please see the sample table at the end of this document for examples of how reagents should be cited.

TABLE FOR AUTHOR TO COMPLETE

Please upload the completed table as a separate document. ***Please do not add subheadings to the Key Resources Table.*** *If you wish to make an entry that does not fall into one of the subheadings below, please contact your handling editor. (****NOTE:*** *For authors publishing in Current Biology, please note that references within the KRT should be in numbered style, rather than Harvard.)*

KEY RESOURCES TABLE

REAGENT or RESOURCE	SOURCE	IDENTIFIER
Antibodies		
Adenylyl Cyclase III (N-14)	Santa Cruz	# sc-32113; RRID:AB_2223118
Arl13b	Proteintech	#17711-1-AP; RRID:AB_2060867
Acetylated α-Tubulin (clone 6-11 B-1)	Sigma	#T6793; RRID:AB_477585
Cytokeratin 19	DSHB	#TROMA-III; RRID:AB_2133570
DNAI2 (1C8)	Sigma	#WH0064446M1; RRID:AB_1841385
GFP	GeneTex	cat# GTX113617; RRID:AB_1950371
Bacterial and Virus Strains		
Biological Samples		
Chemicals, Peptides, and Recombinant Proteins		
N2 supplement	Gibco	Cat# 17502048
B-27 supplement	Gibco	Cat# 17504044
PD0325901	Stemgent	Cat# 04-0006-02
CHIR99021	Stemgent	Cat# 04-0004-02
CK-666	Sigma	Cat# SML0006
Chir99021 (GSK3β inhibitor)	Miltenyl	Cat# 130-103-926
Y-27632 (Rock inhibitor)	Tocris	Cat# 1254
A83-01 (TGFβ inhibitor)	Sigma	Cat# SML0788
FGF10	Peprotech	Cat# AF-100-26
Critical Commercial Assays		
Flp-In Complete System	Life Technologies	Cat# K601001
Antibleaching live cell visualization medium DMEM^{gfp}-2 kit	Evrogen	Cat# MCK02
Deposited Data		
Experimental Models: Cell Lines		
Flp-In 3T3	Life Technoogies	Cat# R76107
Arl13bCerulean-Fucci2a 3T3	This paper	N/A
E14 *R26Arl13b-Fucci2aR* ES	This paper	N/A
Primary ependymal *R26Arl13b-Fucci2a*	This paper	N/A

Primary embryonic fibroblasts *R26Arl13b-Fucci2a*	This paper	N/A
Primary adult bile duct organoids *R26Arl13b-Fucci2a*	This paper	N/A
Experimental Models: Organisms/Strains		
Mouse: *R26Arl13b-Fucci2aR (Cre inducible line)* (*Gt(ROSA)26Sor*$^{tm1.1(CAG-Cerulean/Arl13b,-Venus/GMNN,-Cherry/CDT1)Rmort}$); maintained on a C57BL6/J background	This paper; EMMA and Riken BRC	MGI:6193734
Mouse: *R26Arl13b-Fucci2a (Ubiquitous)* (*Gt(ROSA)26Sor*$^{tm1(CAG-Cerulean/Arl13b,-Venus/GMNN,-Cherry/CDT1)Rmort}$); maintained on a C57BL6/J background	This paper; EMMA and Riken	MGI:6193732
Mouse: *R26-Fucci2a (Ubiquitous)* (*Gt(ROSA)26Sor*$^{tm1.1(CAG-Venus/GMNN,-Cherry/CDT1)Jkn}$); maintained on a C57BL6/J background	Mort et al. 2014; EMMA and Riken BRC	MGI:6193738
Mouse: *CAG:Cre*	Dr D. A. Kleinjan	Unpublished
Mouse: *Sox17-2A-iCre*	Engert et al., 2009	N/A
Oligonucleotides		
Primers used for cloning see S. Table 1	This paper	N/A
Primers used for screening ES cells see S. Table 1	This paper	N/A
Primers used for genotyping mice see S. Table 1	This paper	N/A
Recombinant DNA		
pCDNA5/Frt	Life Technologies	Cat# V601020
POG44	Life Technologies	Cat# V600520
pCAG-H2BCerulean-Fucci2a	R. Mort unpublished	N/A
pCAG-Arl13bCerulean-p2a-Fucci2a	This paper	RDB16059
pCDNA5-CAG-Arl13bCerulean-Fucci2a	This paper	RDB16057
pCAG-Fucci2a	Mort et al., 2014; Riken BRC	RDB13080
pRosa26-CAG-floxNeo-Fucci2a	Mort et al., 2014; Riken BRC	RDB13081
pRosa26-CAG-floxNeo-Arl13bCerulean-Fucci2a	This paper	RDB16058
PGK-Cre	Addgene	#11543
pmKate2-N	Evrogen	cat.# FP182
Software and Algorithms		
Fiji	Schindelin et al., 2012	PMID:22743772
Imaris V9.1	Bitplane	N/A
Nis-Elements AR V4.6	Nikon Instruments	N/A
R-project	R-project	N/A
Other		

TABLE WITH EXAMPLES FOR AUTHOR REFERENCE

REAGENT or RESOURCE	SOURCE	IDENTIFIER
Antibodies		
Rabbit monoclonal anti-Snail	Cell Signaling Technology	Cat#3879S; RRID: AB_2255011
Mouse monoclonal anti-Tubulin (clone DM1A)	Sigma-Aldrich	Cat#T9026; RRID: AB_477593
Rabbit polyclonal anti-BMAL1	This paper	N/A
Bacterial and Virus Strains		
pAAV-hSyn-DIO-hM3D(Gq)-mCherry	Krashes et al., 2011	Addgene AAV5; 44361-AAV5
AAV5-EF1a-DIO-hChR2(H134R)-EYFP	Hope Center Viral Vectors Core	N/A
Cowpox virus Brighton Red	BEI Resources	NR-88
Zika-SMGC-1, GENBANK: KX266255	Isolated from patient (Wang et al., 2016)	N/A
Staphylococcus aureus	ATCC	ATCC 29213
Streptococcus pyogenes: M1 serotype strain: strain SF370; M1 GAS	ATCC	ATCC 700294
Biological Samples		
Healthy adult BA9 brain tissue	University of Maryland Brain & Tissue Bank; http://medschool.umaryland.edu/btbank/	Cat#UMB1455
Human hippocampal brain blocks	New York Brain Bank	http://nybb.hs.columbia.edu/
Patient-derived xenografts (PDX)	Children's Oncology Group Cell Culture and Xenograft Repository	http://cogcell.org/
Chemicals, Peptides, and Recombinant Proteins		
MK-2206 AKT inhibitor	Selleck Chemicals	S1078; CAS: 1032350-13-2
SB-505124	Sigma-Aldrich	S4696; CAS: 694433-59-5 (free base)
Picrotoxin	Sigma-Aldrich	P1675; CAS: 124-87-8
Human TGF-β	R&D	240-B; GenPept: P01137
Activated S6K1	Millipore	Cat#14-486

GST-BMAL1	Novus	Cat#H00000406-P01
Critical Commercial Assays		
EasyTag EXPRESS 35S Protein Labeling Kit	Perkin-Elmer	NEG772014MC
CaspaseGlo 3/7	Promega	G8090
TruSeq ChIP Sample Prep Kit	Illumina	IP-202-1012
Deposited Data		
Raw and analyzed data	This paper	GEO: GSE63473
B-RAF RBD (apo) structure	This paper	PDB: 5J17
Human reference genome NCBI build 37, GRCh37	Genome Reference Consortium	http://www.ncbi.nlm.nih.gov/projects/genome/assembly/grc/human/
Nanog STILT inference	This paper; Mendeley Data	http://dx.doi.org/10.17632/wx6s4mj7s8.2
Affinity-based mass spectrometry performed with 57 genes	This paper; and Mendeley Data	Table S8; http://dx.doi.org/10.17632/5hvpvspw82.1
Experimental Models: Cell Lines		
Hamster: CHO cells	ATCC	CRL-11268
D. melanogaster: Cell line S2: S2-DRSC	Laboratory of Norbert Perrimon	FlyBase: FBtc0000181
Human: Passage 40 H9 ES cells	MSKCC stem cell core facility	N/A
Human: HUES 8 hESC line (NIH approval number NIHhESC-09-0021)	HSCI iPS Core	hES Cell Line: HUES-8
Experimental Models: Organisms/Strains		
C. elegans: Strain BC4011: srl-1(s2500) II; dpy-18(e364) III; unc-46(e177)rol-3(s1040) V.	Caenorhabditis Genetics Center	WB Strain: BC4011; WormBase: WBVar00241916
D. melanogaster: RNAi of Sxl: y[1] sc[*] v[1]; P{TRiP.HMS00609}attP2	Bloomington Drosophila Stock Center	BDSC:34393; FlyBase: FBtp0064874
S. cerevisiae: Strain background: W303	ATCC	ATTC: 208353
Mouse: R6/2: B6CBA-Tg(HDexon1)62Gpb/3J	The Jackson Laboratory	JAX: 006494
Mouse: OXTRfl/fl: B6.129(SJL)-Oxtr$^{tm1.1Wsy}$/J	The Jackson Laboratory	RRID: IMSR_JAX:008471
Zebrafish: Tg(Shha:GFP)t10: t10Tg	Neumann and Nuesslein-Volhard, 2000	ZFIN: ZDB-GENO-060207-1
Arabidopsis: 35S::PIF4-YFP, BZR1-CFP	Wang et al., 2012	N/A
Arabidopsis: JYB1021.2: pS24(AT5G58010)::cS24:GFP(-G):NOS #1	NASC	NASC ID: N70450
Oligonucleotides		
siRNA targeting sequence: PIP5K I alpha #1: ACACAGUACUCAGUUGAUA	This paper	N/A
Primers for XX, see Table SX	This paper	N/A
Primer: GFP/YFP/CFP Forward: GCACGACTTCTTCAAGTCCGCCATGCC	This paper	N/A

Morpholino: MO-pax2a GGTCTGCTTTGCAGTGAATATCCAT	Gene Tools	ZFIN: ZDB-MRPHLNO-061106-5
ACTB (hs01060665_g1)	Life Technologies	Cat#4331182
RNA sequence: hnRNPA1_ligand: UAGGGACUUAGGGUUCUCUCUAGGGACUUAGGGUUCUCUCUAGGGA	This paper	N/A
Recombinant DNA		
pLVX-Tight-Puro (TetOn)	Clonetech	Cat#632162
Plasmid: GFP-Nito	This paper	N/A
cDNA GH111110	Drosophila Genomics Resource Center	DGRC:5666; FlyBase:FBcl0130415
AAV2/1-hsyn-GCaMP6- WPRE	Chen et al., 2013	N/A
Mouse raptor: pLKO mouse shRNA 1 raptor	Thoreen et al., 2009	Addgene Plasmid #21339
Software and Algorithms		
Bowtie2	Langmead and Salzberg, 2012	http://bowtie-bio.sourceforge.net/bowtie2/index.shtml
Samtools	Li et al., 2009	http://samtools.sourceforge.net/
Weighted Maximal Information Component Analysis v0.9	Rau et al., 2013	https://github.com/ChristophRau/wMICA
ICS algorithm	This paper; Mendeley Data	http://dx.doi.org/10.17632/5hvpvspw82.1
Other		
Sequence data, analyses, and resources related to the ultra-deep sequencing of the AML31 tumor, relapse, and matched normal.	This paper	http://aml31.genome.wustl.edu
Resource website for the AML31 publication	This paper	https://github.com/chrisamiller/aml31SuppSite

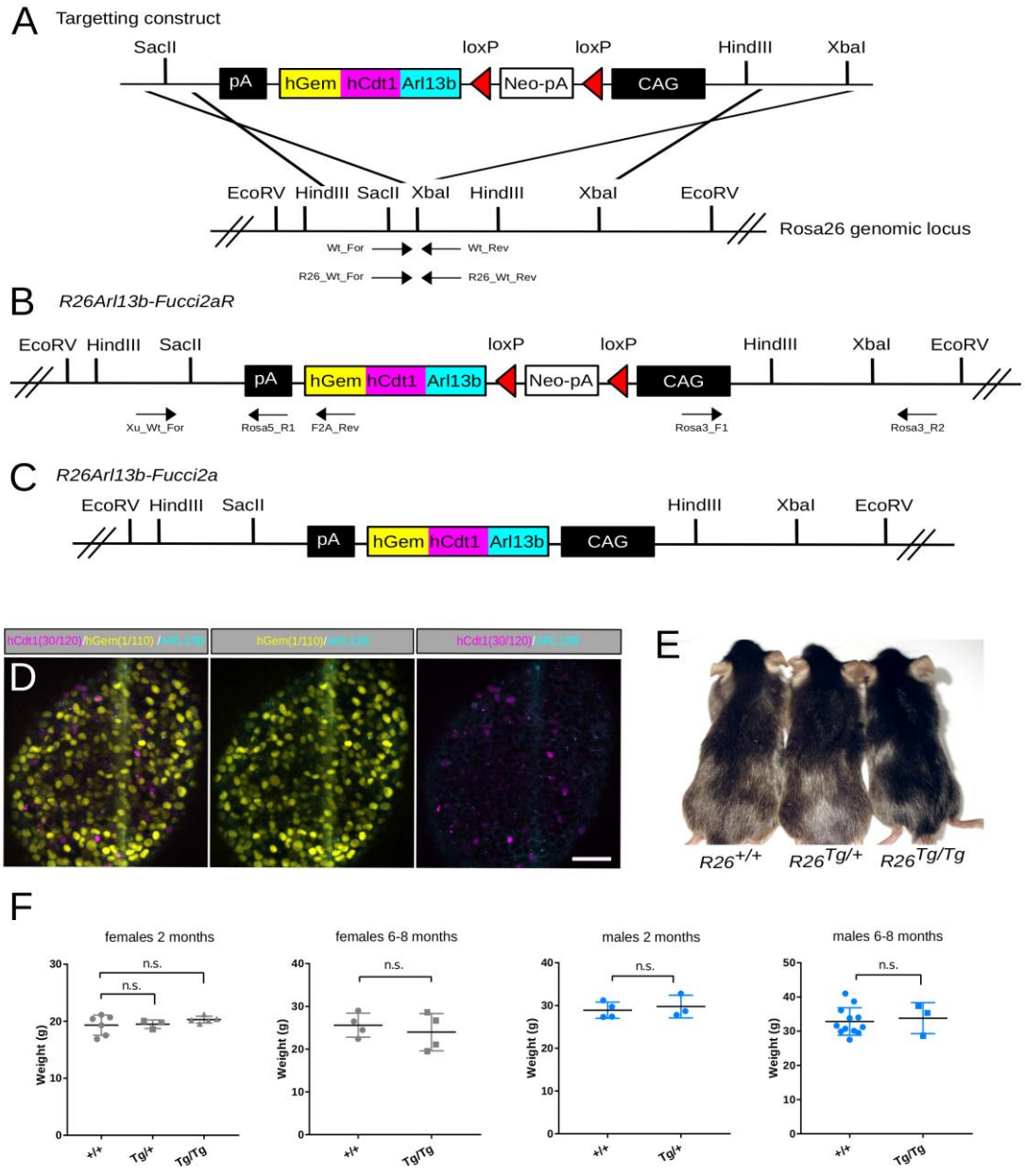

Figure S1, Related to Figure 5. Targeting of Arl13bCerulean-Fucci2a to the *Rosa26* locus in mESCs.

R26Arl13b-Fucci2aR mESCs were generated by homologous recombination of a Cre-recombinase inducible R26Arl13b-Fucci2a targeting construct into the mouse *Rosa26* locus **(A)**. The construct was designed such that expression of the Arl13bCerulean-Fucci2a biosensor is driven by the synthetic CAG promoter and the construct made inducible by inclusion of a loxP flanked neomycin stop cassette between CAG and Arl13bCerulean-Fucci2a sequences. The construct was inserted in the reverse orientation to avoid transcriptional interference between CAG and the endogenous *Rosa26* promoter. **(B)** Successful insertion of the transgene was confirmed by PCR across the 5' and 3' homology arms of the

targeting construct using the primer pairs Xu_Wt_For/Rosa5_R1 (5' targeted band), Rosa3_F1/Rosa3_R2 (3' targeted band) and Wt_For/Wt_Rev (wildtype band - See Methods). Genotyping of mice to confirm we could breed the *R26Arl13b-Fucci2aR* allele to homozygosity was performed in a duplex reaction with the primers R26_Wt_For, R26_Wt_Rev and F2A_Rev (See Methods). The inducible allele was termed *R26Arl13b-Fucci2aR.* **(C)** We activated the transgene in ES cells by transfection with PGK-Cre plasmid followed by selection of fluorescent G418-sensitive clones to yield a recombined constitutive *R26Arl13b-Fucci2a* allele. **(D)** Live images of *R26Arl13b-Fucci2a* mESCs cultured under 2i conditions. **(E)** Constitutively expressing *R26Arl13b-Fucci2a* mice were generated by crossing *R26Arl13b-Fucci2aR* mice with *CAG-Cre* mice. *R26Arl13b-Fucci2a* mice were born at mendelian ratios and were phenotypically indistinguishable from their wild type litter mates. No runting or obesity phenotypes associated with ciliopathies were observed. **(F)** We observed no significant difference (Unpaired t tests, $P > 0.5$ in all cases) in the weights of postnatal males and females at 2 months (females, n = 6 wildtype, 3 heterozygotes, 5 homozygotes; males, n = 4 wildtypes and 3 homozygotes), or at 6-8 months (females, n = 4 wildtype and 4 homozygotes; males, n = 12 wildtypes and 3 homozygotes). Scatterplots include; mean and standard deviation, all values shown. Scale bar in D = 100 µm.

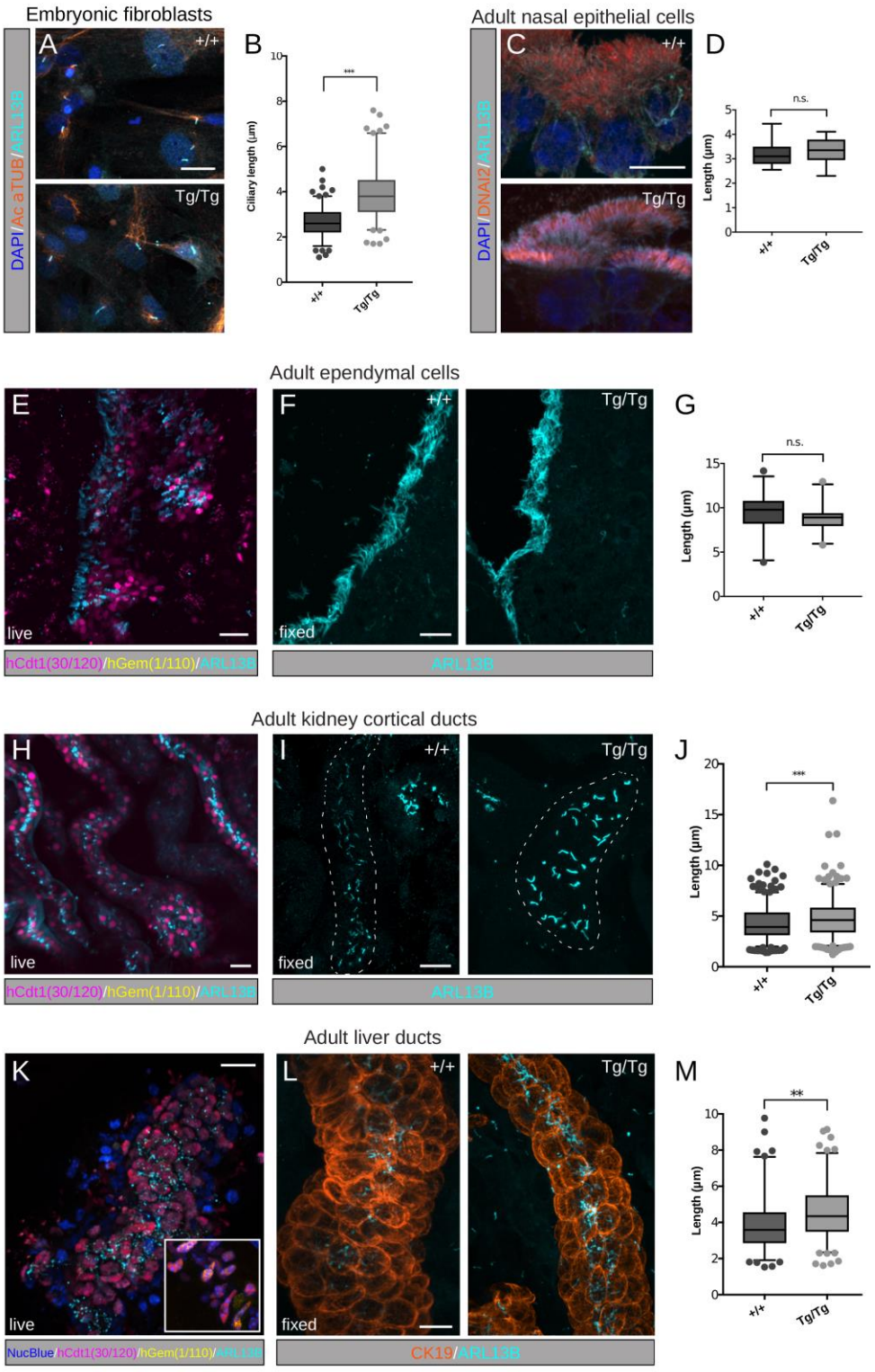

Figure S2, Related to Figure 5. Tissue specific cilia elongation in *R26Arl13b-Fucci2a*$^{Tg/Tg}$ mice. We examined the effect of Arl13b-Cerulean overexpression on cilia length in *R26Arl13b-Fucci2a*$^{Tg/Tg}$ primary cells and adult mice. **(A-B)** Anti-Arl13b staining of primary cilia in *R26Arl13b-Fucci2a*$^{Tg/Tg}$ and wild type mouse embryonic fibroblasts (MEFS) showing that mean cilia length in *R26Arl13b-Fucci2a*$^{Tg/Tg}$ MEFs

(3.955 ± 0.1134 µm, n=121 cilia, n = 1 MEF line, *P* < 0.0001, unpaired t test) is 1.48x greater than in wild type cells (2.675 ± 0.05691 µm, n = 151 cilia, n = 1 MEF line). **(C-D)** Anti-ARL13B (cyan) staining of motile multiciliated (DNAI2: orange) nasal epithelial cells from 6 month old *R26Arl13b-Fucci2a*$^{Tg/Tg}$ (3.33 ± 0.1768 µm, n = 10 cilia, n = 1 animal, P > 0.05, unpaired t test) and wild type (3.268 ± 0.2333 µm, n = 7 cilia, n = 1 animal) mice showing no difference in cilia length. **(E-G)** ARL13B localisation (cyan) in the adult (aged 6 months) brain at the 3rd ventricle showing live expression of the biosensor by vibratome (E), or fixed immunofluorescence of the ependymal cells (F) between *R26Arl13b-Fucci2a*$^{Tg/Tg}$ and wild type mice. Quantitation of length of ARL13B+ cilia (G) revealed no significant difference between *R26Arl13b-Fucci2a*$^{Tg/Tg}$ (8.881 ± 0.338 µm, n = 24 cilia, n = 4 animals, P > 0.05, unpaired t test) and wild type mice (9.414 ± 0.471 µm, n = 27 cilia, n = 4 animals). **(H-J)** ARL13B localisation (cyan) in the adult kidney cortex (aged 2 months) showing live expression from the biosensor by vibratome (H), or fixed immunofluorescence of the cortical ductal cells (I) between *R26Arl13b-Fucci2a*$^{Tg/Tg}$ and wild type mice. Regardless of genotypes ducts showed cilia of variable lengths and intensities such that analysis was confined to ducts (dashed area) with segmentable cilia, shown (J). A significant 1.13 fold increase in primary cilia length was observed between cortical ducts of *R26Arl13b-Fucci2a*$^{Tg/Tg}$ mice (4.789 ± 0.1186 µm, n = 281 cilia, n = 4 animals, P < 0.001, unpaired t test) and wild type (4.251 ± 0.09109 µm, n = 338 cilia, n = 4 animals). **(K-M)** ARL13B localisation (cyan) in bile ducts isolated from adult (aged 4 months) livers showing live expression from the biosensor (K), or fixed whole-mount immunofluorescence where cholangiocytes (CK19: orange) possess long cilia (L). Quantification of ARL13B+ cilia length (M) on cholangiocytes reveals a significant 1.25x increase in length between *R26Arl13b-Fucci2a*$^{Tg/Tg}$ (4.601 ± 0.1337 µm, n = 156 cilia, n = 3 mice, P < 0.05, unpaired t test) and wild type mice (3.975 ± 0.1542 µm, n = 119 cilia, n = 1 animal). Boxplots indicate; 5th percentile, 95th percentile, median and interquartile range, outliers are shown. Scale bar in A = 20 µm, scale bar in C = 10 µm, scale bars in E,F,H,I, and L = 20 µm.

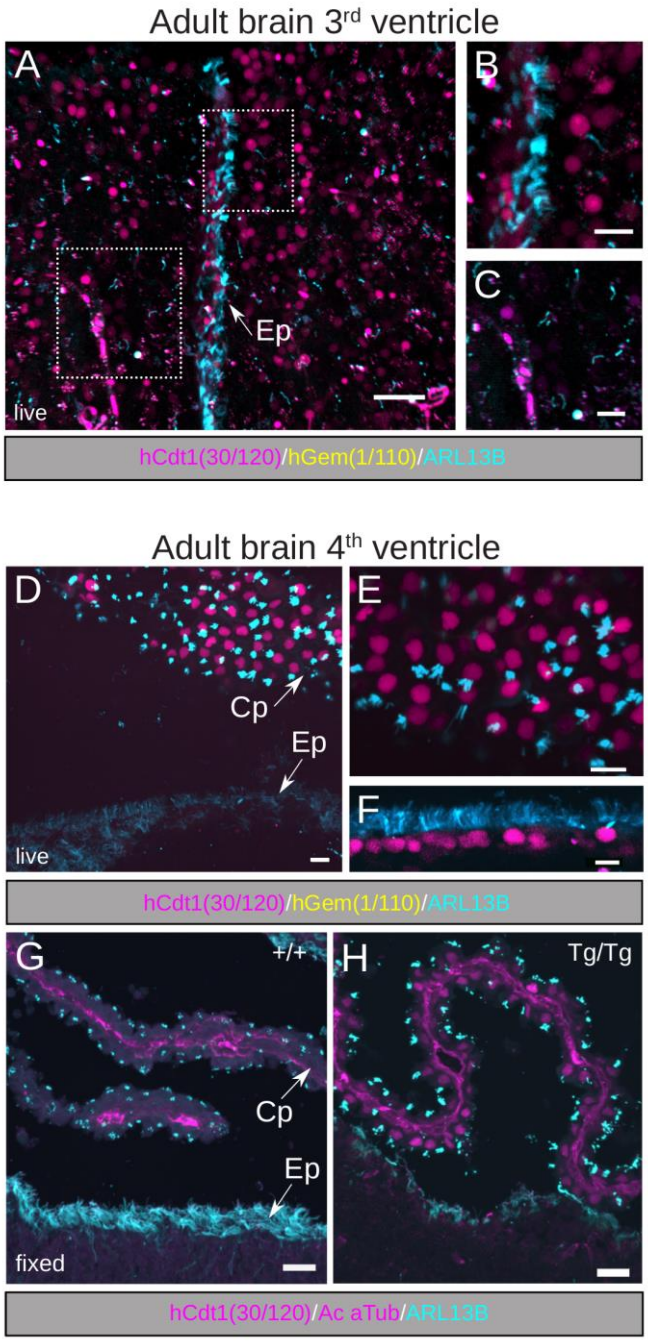

Figure S3, Related to Figure 5. Arl13b-Cerulean sensitively labels diverse cilia types in *R26Arl13b-Fucci2a* mice. Given the challenges of labelling cilia in distinct cell types, especially in the brain, we examined the localisation of ARL13B-Cerulean in live sections from adult brains of *R26Arl13b-Fucci2a*$^{Tg/Tg}$ mice. **(A-C)** ARL13B+ cilia are detected throughout the 3rd ventricle of a *R26Arl13b-Fucci2a*$^{Tg/Tg}$ mouse (aged 6 months). In contrast to the embryonic samples analysed, the majority of cells in adult brain were post-mitotic residing in G0/G1 - labelled with mCherry-hCdt1(30/120). Tufts of ARL13B+ multiciliated ependymal cells (A: Ep and magnified in B) and single primary cilia of neurons (A and magnified in C) are

robustly labelled with ARL13B-Cerulean. **(D-H)** Live imaging in a single field in the adult 4th ventricle (aged 2-months) revealed ARL13B+ cilia on neurons (not shown), as well as motile, multiciliated ependymal cells (D: Ep and F) and in the highly modified, multiciliated cells of the choroid plexus (D: Cp and E) of *R26Arl13b-Fucci2a*$^{Tg/Tg}$ animals (n = 3). **(G-H)** Fixed immunofluorescence with antibodies to ARL13B (cyan) and acetylated α tubulin (magenta) reveal that unlike control samples, *R26Arl13b-Fucci2a*$^{Tg/Tg}$ cilia are very brightly labelled. Note that the choroid plexus is saturated in G despite the image being acquired at a lower exposure than the control sample (H). Ep = ependymal, Cp = choroid plexus, scale bar in A = 50 µm, scale bars in B, C, E, G, H = 20 µm, scale bars in D = 30 µm, and F = 10 µm.

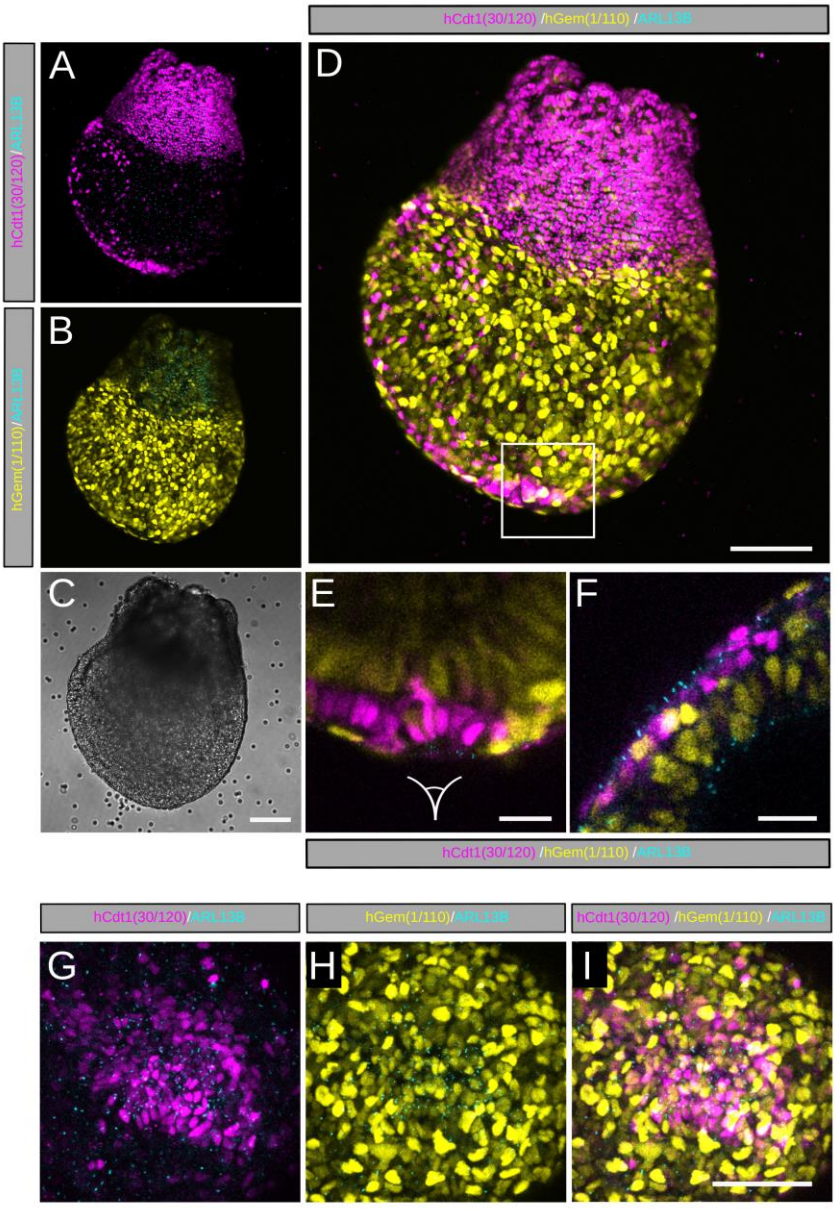

Figure S4, related to Figure 5. The node in E7.5 *R26-Arl13b-Fucci2aR*$^{+/Tg}$*; CAG-Cre*$^{+ve}$ embryos contains a ciliated mCherry-hCdt1 positive population. Ubiquitous Arl13bCerulean-Fucci2a expression was achieved by crossing *R26-Arl13b-Fucci2aR* mice with ubiquitous *CAG-Cre* mice. Confocal imaging was performed on live immobilised E7.5 embryos. **(A-D)** A Z-projection of an e7.5 *R26-Arl13b-Fucci2aR*$^{+/Tg}$*; CAG-Cre*$^{+ve}$ embryo. In all cases (n = 4, *R26Arl13b-Fucci2a*$^{Tg+}$ E7.5 embryos from 3 litters) the extraembryonic ectoderm (proximal) lineages are predominantly non-proliferative (mCherry-hCdt1(30/120) dominates - A) while the embryonic visceral endoderm and epiblast lineages are highly proliferative (mVenus-hGem(1/110) dominates - B).- The majority of cells in the embryonic lineages are

actively cycling in S/G2/M and therefore labelled with mVenus-hGem(1/110), however a collection of mCherry-hCdt1(30/120) positive cells in G1/G0 is evident at the anterior pole of the embryo consistent with the node (box in D). **(E-F)** Single planes of the box in D clearly showing the node as a ciliated population of mCherry-hCdt1(1//110) positive cells projecting into a concave compartment. **(G-I)** Imaging of the node from the anterior perspective (indicated by the eye in E). Scale bar in C-D = 100 μm, scale bars in E = 50 μm, scale bars in G-I = 100 μm.

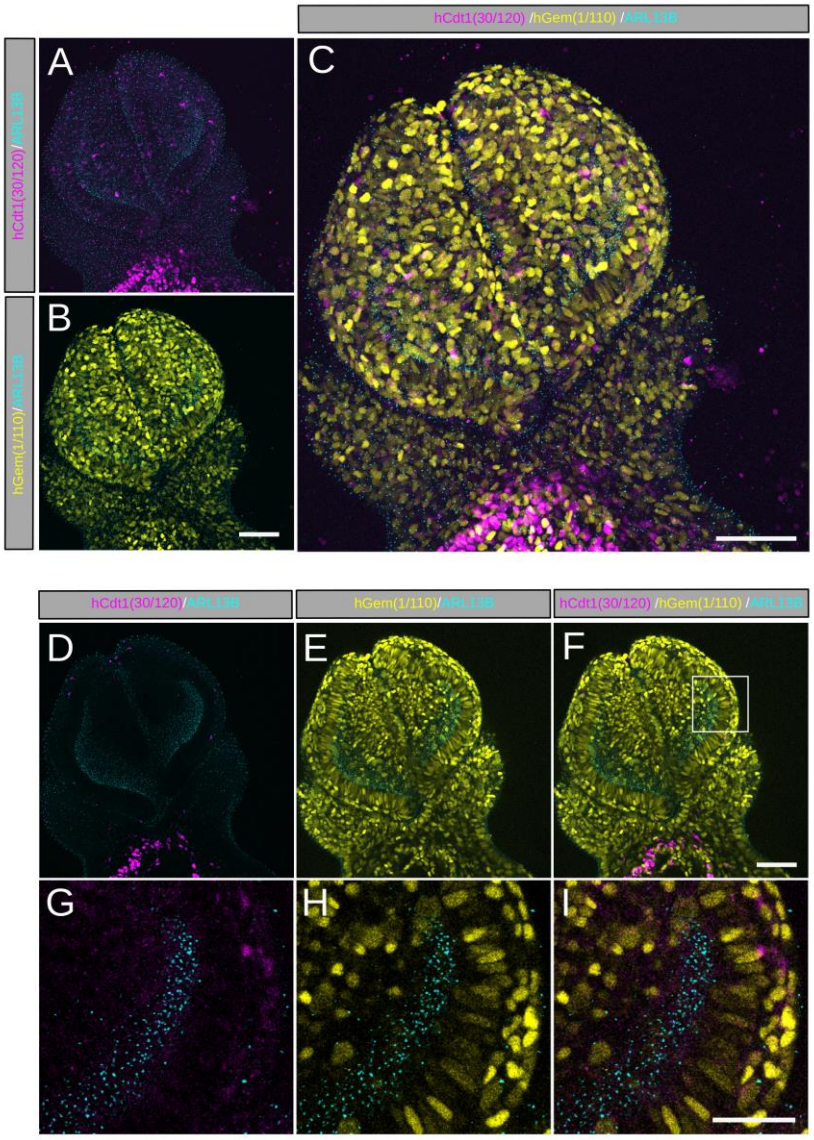

Figure S5, related to Figure 5. Primary cilia are located on the luminal surface of cells lining the lateral ventricles before neurogenesis. (A-C) A Z-projection of an E8.5 prosencephalon from a *R26Arl13b-Fucci2aR*$^{+/Tg}$*; CAG-Cre*$^{+ve}$ embryo. In all cases (n = 8, *R26Arl13b-Fucci2a*$^{Tg+}$ E8.5 embryos from 2 litters) the majority of cells lining and within the future forebrain were identified in S/G2/M phases of the cell cycle labelled with mVenus-hGem(30/120), a large proportion of cells were ciliated regardless of cell cycle stage. **(D-F)** Confocal optical sectioning approximately 40 µm into the embryo revealed ventricles surrounded by the perpendicularly orientated pseudostratified neuroepithelium. **(G-I)** Magnification of ventricular lumen showing a high density of ARL13B-Cerulean labelled cilia projecting into the luminal space. Scale bars in B, C and F = 100 µm, scale bar in I = 50 µm.

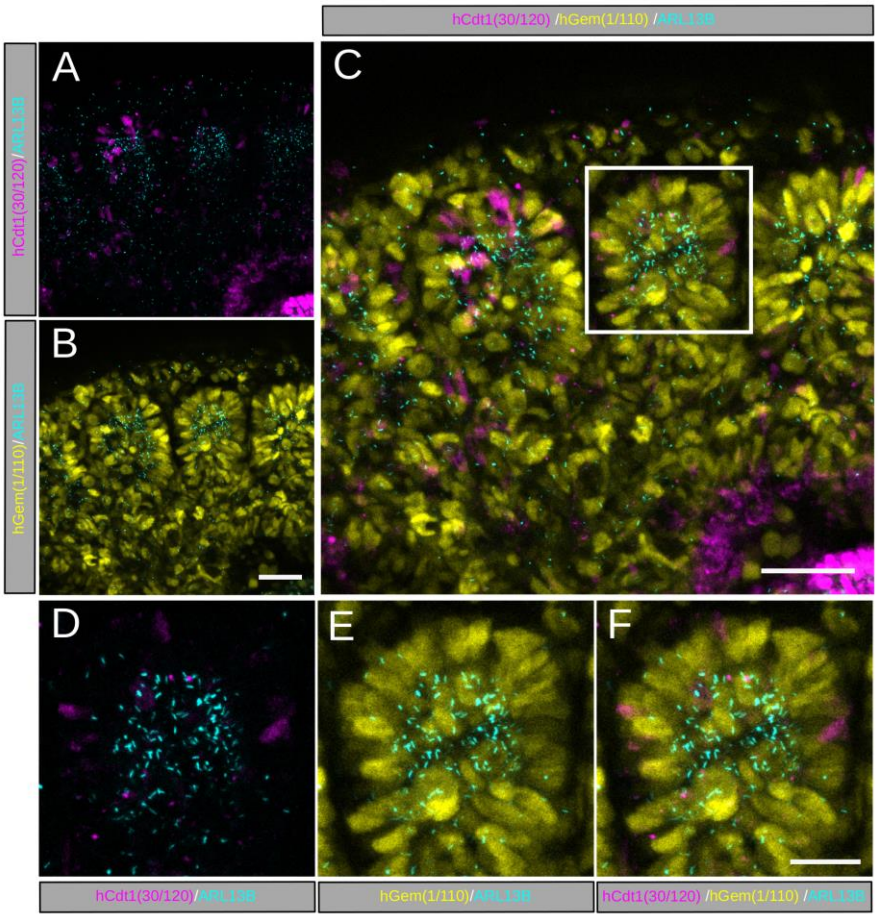

Figure S6, Related to Figure 5. Somites are highly proliferative and contain a high density of primary cilia. (A-C) In all cases (n = 8, *R26Arl13b-Fucci2*$^{Tg+}$ embryos from 2 litters) within the cervical region of E8.5 (5-8 somite stage) *R26-Arl13b-Fucci2aR*$^{+/Tg}$*; CAG-Cre*$^{+ve}$ embryos, somites were recognisable as segmented clusters of proliferating cells predominantly in S/G2/M phases of the cell cycle. **(D-F)** A magnification of a single somite highlights a high density of primary cilia within each somite core. Scale bars in B, C = 100 µm, scale bar in F = 25 µm.

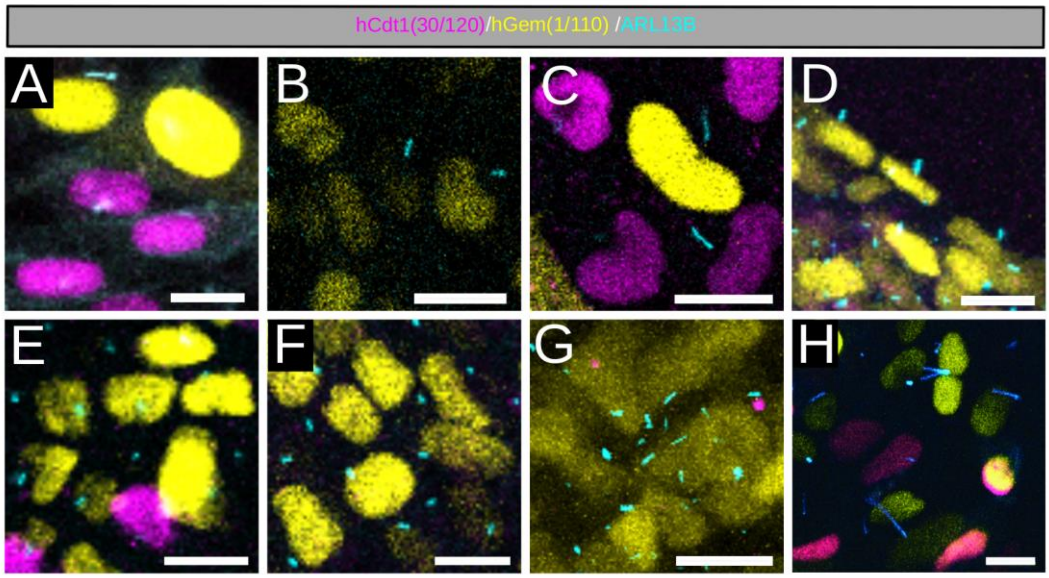

Figure S7, related to Figure 5. Primary cilia are present during S/G2/M phases of the cell cycle *in vitro* and *in vivo*. Confocal images of cells expressing the Arl13bCerulean-Fucci2a transgene indicating ARL13B+ primary cilia located on cells in S/G2/M phases of the cell cycle (yellow - mVenus-hGem(1/110) positive): **(A)** NIH 3T3 cells, **(B)** mouse embryonic stem cells, **(C)** primary ependymal cells, **(D)** the surface of an E8.5 embryo, **(E)** the epiblast of an E7.5 embryo, **(F)** an E8.5 forebrain, **(G)** the centre of an E8.5 somite and **(H)** an adult hepatic ductal organoid. All scale bars = 15 µm.

Table S1, related to STAR Methods: Oligonucleotide sequences used

Name	**Sequence (5' - 3')**
Oligonucleotide sequences used for cloning (restriction endonuclease sites are underlined):	
Arl13b_For	CGGCACAAGCTTATGTTCAGTCTGATGGCCAACTG
Arl13b_Rev	GCCGTCGGATCCCCTGAGATCGTGTCCTGAGCATC
Arl13bCerulean_For	CGGCACACGCGTATGTTCAGTCTGATGGCCAACTG
Arl13bCerulean_Rev	GCCGTCGCGCGCAGGTCCAGGGTTCTCCTCCACGTCTCCAGCCTGCTTCAGCAG
Oligonucleotide sequences used for screening ES cells:	
Wt_For	AAAGTCGCTCTGAGTTGTTAT
Wt_Rev	GGAGCGGGAGAAATGGATATG
Xu_Wt_For	GGCGGACTGGCGGGACTA
Rosa5_R1	CCGTAAATAGTCCACCCATTGACG
Rosa3_F1	GGTGGGCTCTATGGCTTCTG
Rosa3_R2	GGAGTAGTTACTCCACTTTCAAG
Oligonucleotide sequences used for genotyping mice (Wt = 604 bp, Mutant = 880 bp):	
R26_Wt_For	CAAAGTCGCTCTGAGTTGTTATCAG
R26_Wt_Rev	GGAGCGGGAGAAATGGATATGAAG
F2A_Rev	TGGCGGCCGCTCGAGATGAATC